First light for GRAVITY: Phase referencing optical interferometry for the Very Large Telescope Interferometer

Abuter, R.; Accardo, M.; Amorim, A.; Anugu, N.; Ávila, G.; Azouaoui, N.; ... ; Zins, G.

Citation

Abuter, R., Accardo, M., Amorim, A., Anugu, N., Ávila, G., Azouaoui, N., ... Zins, G. (2017). First light for GRAVITY: Phase referencing optical interferometry for the Very Large Telescope Interferometer. *Astronomy & Astrophysics (0004-6361)*, *602*, A94. doi:10.1051/0004-6361/201730838

A&A 602, A94 (2017)
DOI: 10.1051/0004-6361/201730838

Astronomy & Astrophysics

First light for GRAVITY: Phase referencing optical interferometry for the Very Large Telescope Interferometer

GRAVITY Collaboration[⋆]: R. Abuter[8], M. Accardo[8], A. Amorim[6], N. Anugu[7], G. Ávila[8], N. Azouaoui[2], M. Benisty[5],
J. P. Berger[5], N. Blind[10], H. Bonnet[8], P. Bourget[9], W. Brandner[3], R. Brast[8], A. Buron[1], L. Burtscher[1,15], F. Cassaing[11],
F. Chapron[2], É. Choquet[2], Y. Clénet[2], C. Collin[2], V. Coudé du Foresto[2], W. de Wit[9], P. T. de Zeeuw[8,15], C. Deen[1],
F. Delplancke-Ströbele[8], R. Dembet[2], F. Derie[8], J. Dexter[1], G. Duvert[5], M. Ebert[3], A. Eckart[4,14], F. Eisenhauer[1,⋆⋆],
M. Esselborn[8], P. Fédou[2], G. Finger[8], P. Garcia[7], C. E. Garcia Dabo[8], R. Garcia Lopez[3], E. Gendron[2], R. Genzel[1,16],
S. Gillessen[1], F. Gonte[8], P. Gordo[6], M. Grould[2], U. Grözinger[3], S. Guieu[5,9], P. Haguenauer[8], O. Hans[1], X. Haubois[9],
M. Haug[1,8], F. Haussmann[1], Th. Henning[3], S. Hippler[3], M. Horrobin[4], A. Huber[3], Z. Hubert[2], N. Hubin[8],
C. A. Hummel[8], G. Jakob[8], A. Janssen[1], L. Jochum[8], L. Jocou[5], A. Kaufer[9], S. Kellner[1,14], S. Kendrew[3,12], L. Kern[8],
P. Kervella[2,13], M. Kiekebusch[8], R. Klein[3], Y. Kok[1], J. Kolb[9], M. Kulas[3], S. Lacour[2], V. Lapeyrère[2], B. Lazareff[5],
J.-B. Le Bouquin[5], P. Lèna[2], R. Lenzen[3], S. Lévêque[8], M. Lippa[1], Y. Magnard[5], L. Mehrgan[8], M. Mellein[3],
A. Mérand[8], J. Moreno-Ventas[3], T. Moulin[5], E. Müller[3,8], F. Müller[3], U. Neumann[3], S. Oberti[8], T. Ott[1], L. Pallanca[9],
J. Panduro[3], L. Pasquini[8], T. Paumard[2], I. Percheron[8], K. Perraut[5], G. Perrin[2], A. Pflüger[1], O. Pfuhl[1], T. Phan Duc[8],
P. M. Plewa[1], D. Popovic[8], S. Rabien[1], A. Ramírez[9], J. Ramos[3], C. Rau[1], M. Riquelme[9], R.-R. Rohloff[3], G. Rousset[2],
J. Sanchez-Bermudez[3], S. Scheithauer[3], M. Schöller[8], N. Schuhler[9], J. Spyromilio[8], C. Straubmeier[4], E. Sturm[1],
M. Suarez[8], K. R. W. Tristram[9], N. Ventura[5], F. Vincent[2], I. Waisberg[1], I. Wank[4], J. Weber[1], E. Wieprecht[1], M. Wiest[4],
E. Wiezorrek[1], M. Wittkowski[8], J. Woillez[8], B. Wolff[8], S. Yazici[1,4], D. Ziegler[2], and G. Zins[9]

(Affiliations can be found after the references)

Received 21 March 2017 / Accepted 26 April 2017

ABSTRACT

GRAVITY is a new instrument to coherently combine the light of the European Southern Observatory Very Large Telescope Interferometer to form a telescope with an equivalent 130 m diameter angular resolution and a collecting area of 200 m^2. The instrument comprises fiber fed integrated optics beam combination, high resolution spectroscopy, built-in beam analysis and control, near-infrared wavefront sensing, phase-tracking, dual-beam operation, and laser metrology. GRAVITY opens up to optical/infrared interferometry the techniques of phase referenced imaging and narrow angle astrometry, in many aspects following the concepts of radio interferometry. This article gives an overview of GRAVITY and reports on the performance and the first astronomical observations during commissioning in 2015/16. We demonstrate phase-tracking on stars as faint as $m_K \approx 10$ mag, phase-referenced interferometry of objects fainter than $m_K \approx 15$ mag with a limiting magnitude of $m_K \approx 17$ mag, minute long coherent integrations, a visibility accuracy of better than 0.25%, and spectro-differential phase and closure phase accuracy better than 0.5°, corresponding to a differential astrometric precision of better than ten microarcseconds (μas). The dual-beam astrometry, measuring the phase difference of two objects with laser metrology, is still under commissioning. First observations show residuals as low as 50 μas when following objects over several months. We illustrate the instrument performance with the observations of archetypical objects for the different instrument modes. Examples include the Galactic center supermassive black hole and its fast orbiting star S2 for phase referenced dual-beam observations and infrared wavefront sensing, the high mass X-ray binary BP Cru and the active galactic nucleus of PDS 456 for a few μas spectro-differential astrometry, the T Tauri star S CrA for a spectro-differential visibility analysis, ξ Tel and 24 Cap for high accuracy visibility observations, and η Car for interferometric imaging with GRAVITY.

Key words. instrumentation: interferometers – instrumentation: adaptive optics – Galaxy: center – quasars: emission lines – binaries: symbiotic – stars: pre-main sequence

1. Introduction

1.1. From double slit to phase referenced interferometry

About 150 years ago, Fizeau (1868) introduced the concept of stellar interferometry as a double slit experiment. This double slit technique allowed Stephan (1874) to derive strong upper limits for the diameter of stars and was then brought to full fruition by Michelson & Pease (1921) with the measurement of the diameter of Betelgeuse. More than 50 years later, Labeyrie (1975) was able to demonstrate the interference between two telescopes as the basis for modern optical interferometry. At this time radio interferometry was already well advanced with first imaging synthesis arrays and with very long baseline interferometry (VLBI) for highest angular resolution and astrometry (see, e.g., Thompson et al. 2017, and references therein). The discoveries from radio interferometry – for example, the imagery of Cygnus A (Hargrave & Ryle 1974) and the observations of apparent superluminal motion in 3C 273 (Pearson et al. 1981)

[⋆] GRAVITY is developed in a collaboration by the Max Planck Institute for extraterrestrial Physics, LESIA of Paris Observatory/CNRS/UPMC/Univ. Paris Diderot and IPAG of Université Grenoble Alpes/CNRS, the Max Planck Institute for Astronomy, the University of Cologne, the Centro Multidisciplinar de Astrofísica Lisbon and Porto, and the European Southern Observatory.

[⋆⋆] Corresponding author: F. Eisenhauer
e-mail: `eisenhau@mpe.mpg.de`

– also set the direction for optical/infrared interferometry. But it needed significant technical advances in technology – to name a few: detectors, optics, electronics, computers, and lasers – to arrive at modern optical/infrared interferometers, for example, the Mark III stellar interferometer (Shao et al. 1988).

The largest current optical/infrared interferometers are the Georgia State University's Center for High Angular Resolution Astronomy (CHARA) interferometer with six 1 m diameter telescopes, and the European Southern Observatory (ESO) Very Large Telescope Interferometer (VLTI, Haguenauer et al. 2012), combining either up to four 8 m diameter unit telescopes (UTs) or up to four movable 1.8 m diameter auxiliary telescopes (ATs). In comparison with interferometers at radio wavelengths, optical/near-infrared interferometry is disadvantaged by three fundamental limitations: (1) the practical and fundamental limitations for a broad-band heterodyne detection – pioneered and applied for wavelengths down to 10 μm with the infrared spatial interferometer (ISI) and its prototype (Johnson et al. 1974; Hale et al. 2000) –, and the atmospheric turbulence leading to (2) only partial coherence of the beams of each telescope, and to (3) short coherence times for the interference between the telescopes.

The effect of the variable wavefront coherence of each telescope is notoriously difficult to cope with at shorter wavelengths. This problem was overcome in the 1990s with the introduction of single-mode fibers in the fiber linked unit for optical recombination (FLOUR, Coudé du Foresto et al. 1998), which spatially filter the wavefronts corrugated by the atmospheric turbulence, and allow for visibility accuracies as good as a few 0.1% (Perrin et al. 2004). In the case of a large telescope, adaptive optics are necessary to maximize the coupling to the single mode fibers. This was first done at the VLTI with the multi-application curvature adaptive optics (MACAO, Arsenault et al. 2003).

The second problem of atmospheric turbulence, the short coherence time between two telescopes, limits the detector integration time to typically less than 100 ms in the astronomical K-band (1.95–2.45 μm), and because of detector-read noise, to objects brighter than $m_K \approx 10$ mag for broad-band observation even for 10 m class telescopes (Weigelt et al. 2012; Kishimoto et al. 2011), and significantly brighter objects for high spectral resolution. The technology to stabilize the optical path difference (OPD) between two telescopes to a fraction of a wavelength is called phase-tracking or fringe-tracking[1]. Phase-tracking was first demonstrated by Shao & Staelin (1980), used on the Mark III interferometer (Shao et al. 1988) and the Palomar Testbed Interferometer (PTI, Colavita et al. 1999), and later, for example, at the Keck Interferometer (KI, Colavita & Wizinowich 2003) and with the Fringe-tracking instrument of Nice and Torino (FINITO, Gai et al. 2003) at the VLTI. Because these closed loop systems require significantly shorter detector integration times of typically a few ms, the broad-band sensitivity itself does not improve, but fringe-tracking boosts the sensitivity for parallel high-spectral resolution observations with long, coherent integrations. Fringe-tracking also opens up the possibility of observing objects close to a reference star with long coherent exposures, greatly increasing also the broad-band limiting magnitude, and at the same time providing the phase reference for precise narrow angle astrometry (Shao & Colavita 1992), visibility measurements (Quirrenbach et al. 1994), and radio-VLBI-like imaging (Alef 1989). Such off-axis fringe-tracking was implemented in PTI (Colavita et al. 1999), the dual field phase referencing instrument (Woillez et al. 2014) for the KI, and the Phase-Referenced Imaging and Micro-arcsecond Astrometry facility (PRIMA, Delplancke 2008) for the VLTI. These instruments demonstrated the potential of this technique with 10 μas-astrometry (Lane & Muterspaugh 2004) and interferometry of objects as faint as $m_K \approx 12.5$ mag (Woillez et al. 2014), but to date have not yet been exploited scientifically.

1.2. From astrophysical questions to GRAVITY

Inspired by the potential of phase-referenced interferometry to zoom in on the black hole in the Galactic center and to probe its physics down to the event horizon (Paumard et al. 2008), we proposed in 2005 a new instrument named GRAVITY as one of the second generation VLTI instruments (Eisenhauer et al. 2008). At its target accuracy and sensitivity, GRAVITY will also map with spectro-differential astrometry the broad line regions of active galactic nuclei (AGN), image circumstellar disks in young stellar objects and see their jets evolve in real time, and detect and characterize exo-planets especially around low mass stars and binaries – in short we will "Observe the Universe in motion" (Eisenhauer et al. 2011).

The instrument derives its design and optimization from focusing on the science themes mentioned above: K-band operation – both wavefront sensor and beam combiner – for optimum resolution and sensitivity in highly dust-extincted regions and access to the most important near-infrared line diagnostics including Brγ, He I,II, H_2, and the CO band heads; fringe-tracking with a limiting magnitude fainter than $m_K \approx 10$ mag for the Galactic center phase reference stars and giving access to the brightest AGN and low-mass T Tauri stars; a broad-band limiting magnitude fainter than $m_K \approx 16$ mag – when fringe-tracking off-axis on a bright reference star – to trace flares around the Galactic center black hole and the fast motions of stars at distances smaller than 100 mas; a medium $R = \lambda/\Delta\lambda \approx 500$ and high $R \approx 4500$ spectral resolving power to probe extragalactic and circumstellar velocities, respectively; and narrow angle astrometry well below 100 μas with a goal of 10 μas to probe general relativistic effects around the Galactic center black hole and to potentially detect planetary mass companions around nearby stars.

Following a one-year phase-A study, the instrument was selected at the end of 2007. We presented the preliminary and final designs in 2009/10 and 2011/12, respectively. The beam-combiner instrument was shipped to Paranal in mid 2015, with the four infrared wavefront sensors following between February and July 2016.

1.3. First light for GRAVITY

One year after the start of the VLTI upgrade for the 2nd generation instruments (Gonté et al. 2016a), we began the commissioning of the GRAVITY beam combiner instrument with the four ATs in November 2015[2]. The commissioning with the four UTs started in May 2016. The first infrared wavefront sensor saw first starlight in April 2016. The full GRAVITY instrument with all infrared wavefront sensors had its first observations with the four UTs in September 2016. Science verification – following proposals from the community and with open data access – with

---

[1] The term fringe-tracking is also used in a wider sense for stabilizing the OPD between the telescopes to within a coherence length $\Lambda = R\lambda$, where $R = \lambda/\Delta\lambda$ is the spectral resolving power of the interferometer.

[2] http://www.eso.org/public/news/eso1601/

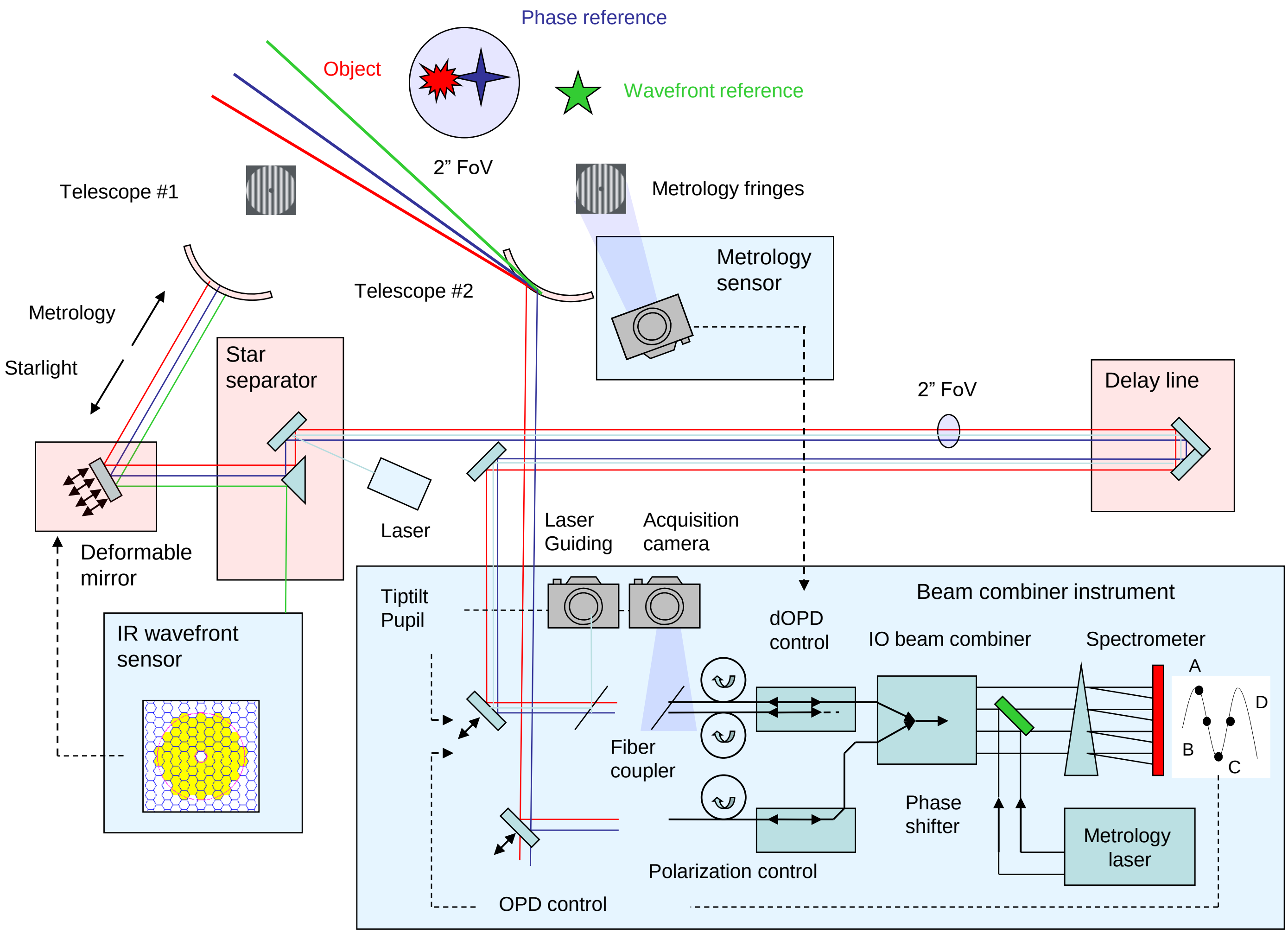

Fig. 1. Overview and working principle of GRAVITY: the instrument coherently combines the light of the four 8 m UTs of the VLTI or the four 1.8 m ATs. It provides infrared wavefront sensing to control the telescope adaptive optics, two interferometric beam combiners – one for fringe-tracking and one for the science object –, an acquisition camera and various laser guiding systems for beam stabilization, and a dedicated laser metrology to trace the optical path length differences for narrow angle astrometry. The overview illustrates the light path and location of the various subsystems. For clarity, we show only two telescopes, one beam combiner, and one wavefront sensor. The wavefront sensor star (green) can be outside the VLTI field of view. Depending on the brightness of the science object (red), the fringe tracker is either fed by a beam splitter, or – as illustrated in this figure – by a bright off-axis phase reference star (blue). The GRAVITY subsystems (light blue boxes) are embedded and take advantage of the already existing VLTI infrastructure (light red boxes).

the ATs was carried out in June and September 2016, with first results published in, for example, Le Bouquin et al. (2017) and Kraus et al. (2017). Science operation with the ATs started in October 2016, followed by the UTs in April 2017.

This paper provides a comprehensive description of the instrument (Sect. 2) and presents a set of early observations that illustrate its power (Sect. 3). The detailed description of the instrument subsystems and software, and of the analysis and interpretation of the observations, will be given in several forthcoming papers.

2. The GRAVITY instrument

2.1. Overview and working principle

The goal of the GRAVITY design is to provide a largely self-contained instrument for phase-referenced imaging of faint targets and precise narrow angle astrometry. Figure 1 illustrates the GRAVITY concept. For clarity, only two of four telescopes, that is, one out of six baselines, are shown.

The working principle of GRAVITY is as follows: a bright wavefront reference star (e.g., in the Galactic center this is GC IRS 7, a $m_K = 6.5$ mag star at $5.5''$ separation from the supermassive black hole) outside the $2''$ field-of-view of the VLTI is picked with the PRIMA star separator (Delplancke et al. 2004) and imaged onto the GRAVITY Coudé infrared adaptive optics (CIAO) wavefront sensors. The wavefront correction is applied using the MACAO deformable mirrors of the UTs. The $2''$ field-of-view of the VLTI contains both the science target (Sgr A*) and the phase reference star (GC IRS 16C, $1.23''$ separation, $m_K = 9.7$ mag). Both objects are re-imaged via the main delay lines (Derie 2000) to the GRAVITY beam combiner instrument. Laser guiding beams are launched at the star separator and telescope spider arms to trace the tip-tilt and pupil motion, respectively, within the VLTI beam relay. The GRAVITY beam combiner instrument has internal sensors and actuators to analyze these beams and to apply the corresponding corrections.

Longer-term image drifts of the object are compensated with the help of the internal acquisition camera (working at H-band, 1.45−1.85 μm). This camera also analyzes the signal from the pupil-guiding laser beams launched at the telescope spider arms. The fiber coupler de-rotates the field, splits the light of the two stars, and injects it into single-mode fibers. A rotating half-wave plate is used to control the linear polarization of the light. A fiber control unit including rotators and stretchers aligns the polarization for maximum contrast, and compensates the differential optical path difference (dOPD) between the phase reference star and science object caused by their angular separation on sky. The beam combiner itself is implemented as an integrated optics chip with instantaneous fringe sampling. The bright reference star feeds the fringe tracker, which measures the phase and group delay from six spectral channels across the K-band. The OPD correction is applied to an internal piezo-driven mirror, stabilizing the fringes of both the reference star and the faint science object. The science spectrometer is optimized for longer, background-limited integration times of faint objects, and offers a variety of operation modes, including broad-band (ten spectral pixel) observations and $R \approx 500$ and $R \approx 4500$ resolution spectroscopy. Both the fringe tracker and the science spectrometer can be used with a Wollaston prism to split and simultaneously measure two linear polarization states. The dOPD between the science and reference beams is measured with a laser metrology system. The laser light is back-propagated from the GRAVITY beam combiners covering the full beam up to above the telescope primary mirror. The metrology is implemented via phase-shifting three-beam interferometry and measured by photodiodes mounted on the telescope spider arms. A dedicated calibration unit simulates the light from two stars and four telescopes, and provides all functions to test and calibrate the beam combiner instrument.

GRAVITY provides simultaneously for each spectral channel the visibility of the reference and science object, and the differential phase between reference and science object. The GRAVITY data can be used for interferometric imaging exploring visibilities and closure phases obtained simultaneously for six baselines, and for astrometry using the differential phases and group delays. The spatial frequency coverage can be further extended taking advantage of the earth rotation, and in the case of the ATs, by relocating the telescopes.

2.2. Beam combiner instrument

The beam combiner instrument is installed in the VLTI interferometric laboratory located at the center of the Paranal observatory. Most subsystems are hosted in a cryostat for optimum stability, cleanliness, and thermal background suppression (see Fig. 2).

2.2.1. Cryostat

The cryostat (Haug et al. 2012) provides the required temperatures for the various subunits of the beam combiner instrument. The temperatures range from about 80 K for the detectors and spectrometers, 200 K for the integrated optics, 240 K for the optical bench and fiber couplers, and up to 290 K for the metrology injection units. The bath-cryostat is cooled with liquid nitrogen and makes use of the gaseous exhaust to cool the intermediate 240 K temperature subsystems. All temperature levels are actively stabilized with electric heaters. The cold bench is supported separately from the vacuum vessel and liquid nitrogen reservoir to minimize vibrations within the instrument.

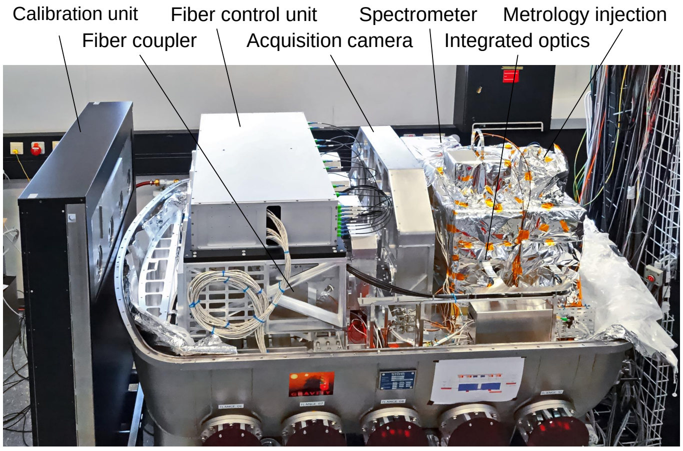

Fig. 2. Beam combiner instrument: the photograph shows the instrument with the vacuum vessel removed to expose the subsystems. The light from the four telescopes enters from the left. The fiber couplers are located in the left part of the instrument below the fiber control unit. The acquisition camera and the receivers for the tip/tilt laser stabilization are seen in the middle of the instrument. The black cables are single-mode fibers connecting the fiber control unit with the fiber couplers and the integrated optics beam combiner. These integrated optics beam combiners are mounted to the two spectrometers – wrapped in shiny super isolation – seen on the right. The laser metrology is injected through the little "huts" – also wrapped in super isolation – on top of the spectrometers. The warm calibration unit is the black box on the very left.

2.2.2. Fiber coupler

The main purpose of the fiber coupler (Pfuhl et al. 2014) is to feed the light from the reference and science objects into the fibers. Figure 3 shows the optical design for one of the four units. Every fiber coupler provides a number of functions. First, a motorized K-mirror corrects the field-rotation induced by the VLTI optical train. After that, a motorized half-wave plate allows for the independent rotation of the linear polarization. Two piezo-driven mirrors provide tip-tilt-piston and lateral pupil control, respectively. They are part of an off-axis parabolic mirror relay optics, which focuses the starlight onto a roof-prism. One part of the roof-prism is fully reflective to completely separate the phase reference and the science star light; another part of the roof is a beam-splitter to send half of the light to the fringe tracker and science spectrometer, respectively. Two separate relay optics then couple the phase reference and science starlight into their respective fibers, which are mounted on piezo-driven three-axis stages to pick the objects and adjust the focus. The acquisition and guiding camera is fed via a dichroic beam splitter. To ease the alignment, a retro-reflector behind the dichroic beam splitter allows for imaging of the fiber entrance onto the acquisition camera. Behind the dichroic beam splitter, there is also a multi-mode fiber to pick up part of the laser metrology light as a feedback signal for controlling the fiber differential delay lines.

2.2.3. Single-mode fibers and fiber control unit

GRAVITY uses fluoride-glass single-mode fibers to transport the light from the fiber couplers to the integrated optics, where the beams from the four telescopes interfere. The fibers also spatially filter the wavefronts corrugated by the atmospheric turbulence. As such the phase fluctuations are traded against photometric fluctuations, which are measured by the beam combiner to calibrate the coherence losses. GRAVITY uses weakly birefringent fluoride-glass fibers (beat lengths between 313 m

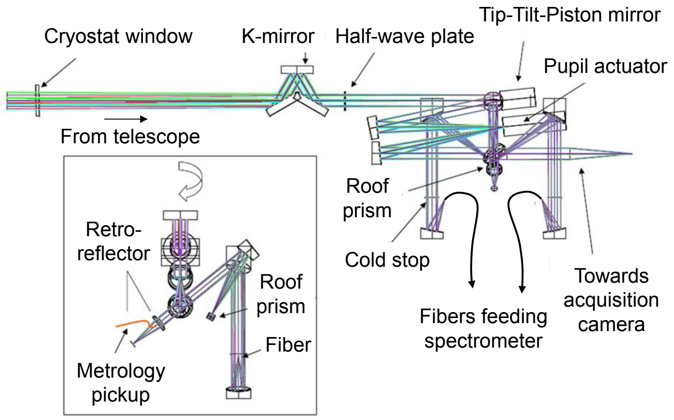

Fig. 3. Fiber coupler: schematic shows side and front views of optical design for one of the four fiber couplers. The fiber couplers provide all optics and actuators to rotate and stabilize the beam, to split the light of the fringe tracker and science objects, and to optimally couple the light into the single-mode fibers. In addition, the fiber coupler contains several supplementary functions, including a metrology pickup to control the fiber differential delay lines, a retro-reflector to image the fiber input on the acquisition camera, and motorized half-wave plates for co-aligning the polarization.

and 1074 m) such that for the fiber length of 20.5 m to 22 m per beam an intrinsic maximum contrast higher than 98.2% can be achieved without splitting polarizations to ensure maximum sensitivity on faint objects. The fiber lengths have been matched to simultaneously minimize optical path differences and differential dispersion between the four beams of the fringe tracker and science beam combiner, respectively. Respective maximum values for each of the six baselines are 0.9 mm and 5.7 μrad cm^2, which correspond to a contrast loss of less than 5% for the low spectral resolution mode (see Sect. 2.2.5) of GRAVITY, and negligible contrast losses at medium and high spectral resolution.

In addition to spatial filtering, the fibers of GRAVITY are used to control the dOPD between the science and phase reference objects and the polarization of the transported light (see Fig. 4). The fiber differential delay lines use between 15.9 m and 17.5 m of fiber wrapped on two half-spools whose distance can be varied with a 100 μm stroke piezo translation stage. The variable stretching of the fibers allows us to produce variable delays up to 6 mm. The delays are controlled with a combination of strain gauge feedback for absolute positioning with few 10 μm accuracy and the GRAVITY metrology system for nanometer relative accuracy.

The second kind of actuators are fiber polarization rotators in which one meter of fiber is twisted with a stepper motor to rotate the polarization and match the polarization axes for all GRAVITY baselines. The maximum stroke is slightly larger than 180° with an accuracy of 0.2°. The fiber differential delay lines and the fiber polarization rotators are connected to the fiber coupler fibers and feed the fiber bundle towards the integrated optics chip. The throughput of the whole fiber chain excluding coupling losses exceeds 87.5%. The fibers and fiber control unit were developed by Le Verre Fluoré in collaboration with the Laboratoire d'Études Spatiales et d'Instrumentation en Astrophysique (LESIA) and the Institut de Planétologie et d'Astrophysique de Grenoble (IPAG).

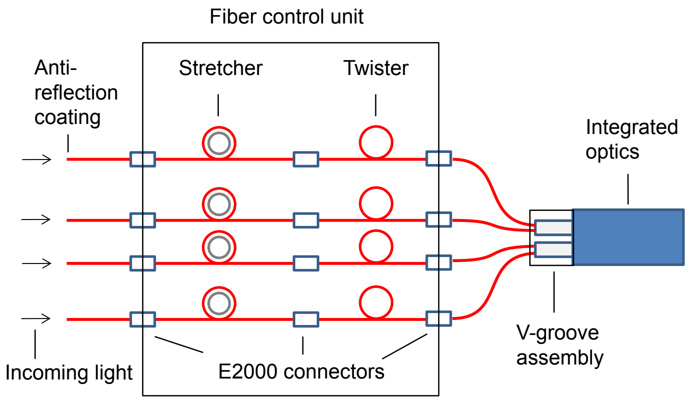

Fig. 4. Single-mode fibers and fiber control unit: schematic shows the various fiber subsections and functions. The entrance of the fibers are anti-reflection coated. The optical path length is adjusted by piezo-driven fiber coils. The direction of linear polarization is aligned by motorized fiber twisters. The fibers of these subsections are connected through optimized E2000 connectors. The integrated optics beam combiner – operated at 200 K – is connected through a dedicated V-groove assembly.

2.2.4. Integrated optics

The two beam combiners (Jocou et al. 2014) for the reference star and the science object are integrated optics (IO) chips – the optical equivalent of electronic integrated circuits. These beam combiners are directly fed by the single-mode fibers, and provide instantaneous fringe sampling for all six baselines. Figure 5 shows a photograph and a schematic of the GRAVITY integrated optics.

The fringe coding is a pair-wise simultaneous ABCD sampling, which provides in its four outputs the interference intensity at roughly 0°, 90°, 180°, and 270° relative phase shift, respectively. As opposed to earlier implementations of the ABCD scheme (e.g., Colavita et al. 1999), which apply a temporal modulation to sample the fringe, the GRAVITY beam combiner gives an instantaneous measurement of the fringe parameters. This beam combination is implemented as a double Michelson beam combiner: two successive single-mode splitters with theoretical coupling ratios of 66/33 and 50/50, respectively, split the light from each telescope into three beams with the same intensity, achromatic $\frac{\pi}{2}$ phase shifters introduce the above mentioned relative phase shifts, and two beam combiners – X-couplers – create the four outputs in phase quadrature. The beam combiners have therefore 24 outputs – six baselines with four fringe samples each – feeding the spectrometers. The integrated optics beam combiners are operated at 200 K to avoid thermal background.

The GRAVITY integrated optics beam combiners have been produced by plasma-enhanced chemical vapor deposition of phosphor-doped silica on a silicon wafer and manufactured by the Laboratoire d'Électronique des Technologies de l'Information (CEA/LETI). This technology is widely used in telecommunications up to a wavelength of 1.6 μm and has been successfully applied in astronomical interferometry in the *H*-band (Le Bouquin et al. 2011). The GRAVITY challenge was to port this technology to longer wavelengths with a dedicated development program, first with a series of prototypes for individual functions, and then for the full integrated optics. The transmission ranges from ≈68% for short wavelengths around 2.0 μm to ≈23% at long wavelengths around 2.45 μm, with a mean a transmission of >54% in this wavelength range.

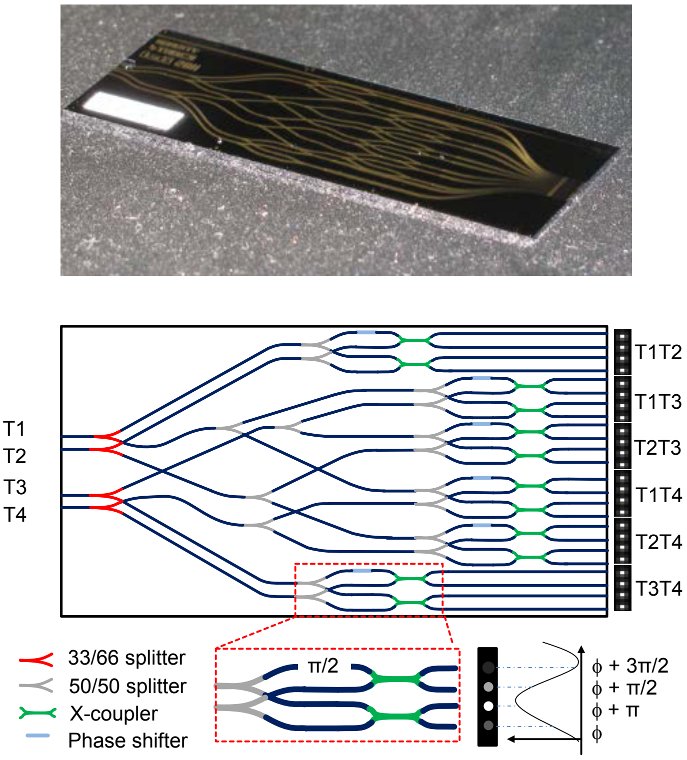

Fig. 5. Integrated optics beam combiner: the actual interference happens in an etched silica-on-silicon integrated optics chip. The *top panel* shows a photograph of the GRAVITY integrated optics, the *lower panel* the design of the circuit. The integrated optics contain all functions (dark blue: waveguides, red and gray: beam splitter, light blue: phase shifter, green: X coupler) for a pairwise combination of the four telescopes and fringe sampling. The light from the four telescopes T1 ... T4 is fed by single-mode fibers from the left, the output on the right is the interference of the six telescope combinations for a relative phase shift of 0°, 90°, 180°, and 270°, respectively.

2.2.5. Spectrometer

GRAVITY includes two spectrometers (Straubmeier et al. 2014) for the 1.95–2.45 μm wavelength range for the simultaneous detection of the interferometric signals of two astronomical sources: a potentially faint science object and a brighter fringe-tracking object. To minimize the thermal background, the two spectrometers are operated at 85 K. The optical input of each spectrometer consists of the 24 output channels of the respective integrated optics beam combiner. The fringe-tracking spectrometer is optimized for high readout frame rates in the kilohertz (kHz) regime at low spectral resolution with six spectral pixels, while the science spectrometer is optimized for second- to minute-long integration times and allows us to select from three spectral resolutions of $R \approx 22$, $R \approx 500$, and $R \approx 4500$. Both spectrometers can be operated with or without splitting the linear polarization of the star light. The spectrometer also feeds the laser metrology backwards into the integrated optics, through which it is propagated up to the four telescopes.

The optical design of both spectrometers (see Fig. 6) is mostly identical and differs only in the dispersive elements, the angle of the Wollaston prisms, and the $F\#$ of the cameras. The beams from the 24 outputs of the integrated optics beam combiner are collimated by a four-lens system with $F\# \approx 2.27$ to a beam diameter of 24 mm. After passing the dichroic of the laser metrology injection (the dichroic is only reflective at the laser wavelength of 1.908 μm) the light is filtered by an astronomical K-band filter and two filters to block the powerful 1.908 μm metrology laser with a total optical density of $OD \geq 16$. Following the pupil stop, the light is spectrally dispersed. In the fringe-tracking spectrometer the dispersion is achieved by a double prism made from barium fluoride and fused silica. In the science spectrometer the low spectral resolution uses a single fused silica prism, while the medium and high spectral resolution are produced by directly ruled grisms made from zinc selenide. A deployable Wollaston prism made from magnesium fluoride allows for the splitting of the orthogonal directions of linear polarization. The camera optics of the science spectrometer is a four-lens system; the fringe tracker camera optics is a three-lens system including two aspherical surfaces. We chose a $F\# \approx 5.5$ for the science spectrometer to spread the high resolution spectrum over the full 2048 pixel of a HgCdTe Astronomical Wide Area Infrared Imager (HAWAII) 2RG detector array (see Sect. 2.2.9 on the detectors used in GRAVITY). The fringe-tracking spectrometer camera has an $F\# \approx 1.8$ to achieve an ensquared energy of >90% within a single $24 \times 24\,\mu\text{m}^2$ pixel of the SAPHIRA detector array.

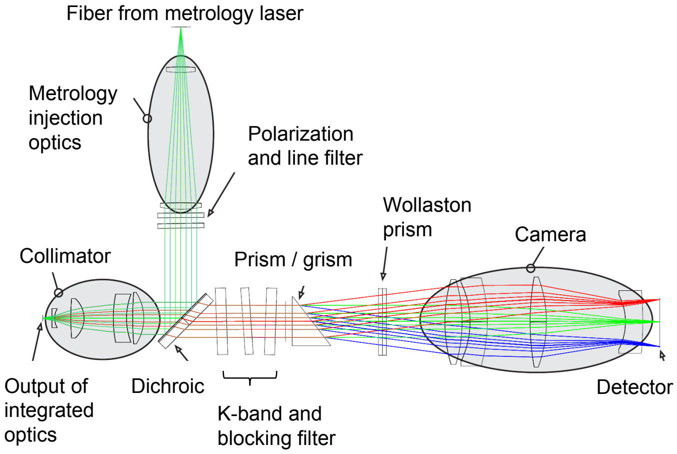

Fig. 6. Optical design of the two spectrometers of GRAVITY for the example of the science spectrometer in high spectral resolution polarimetric configuration. The dispersive elements and the Wollaston prism are mounted on cryogenic exchange mechanisms to provide user selectable configurations. The detector is mounted on cryogenic linear stages to allow for proper focusing.

The metrology injection is identical in both spectrometers. Two metrology fibers – enough to feed all four telescopes, because the laser light is split in the beam-combiner – per spectrometer are each mounted on piezo-driven three-axis positioners on top of the spectrometer housing. The emerging beams are collimated by a two-lens aspheric system with $F\# \approx 4.35$ to a beam diameter of 24 mm. After a pupil stop, the beams pass a 1.908 μm narrow-band line filter and a linear polarization filter, before they are reflected by the 45° dichroic and focused by the spectrometer collimator in reverse direction on two outputs of the integrated optics beam combiner. From here the metrology laser traces exactly the stellar light path back through the integrated optics, fibers, and optics up to the telescopes.

2.2.6. Beam combiner instrument throughput

We measured the optical throughput of the beam combiner instrument with a blackbody light source installed at the instrument input. Figure 7 shows the optical throughput of the beam combiner instrument without the Wollaston prisms and

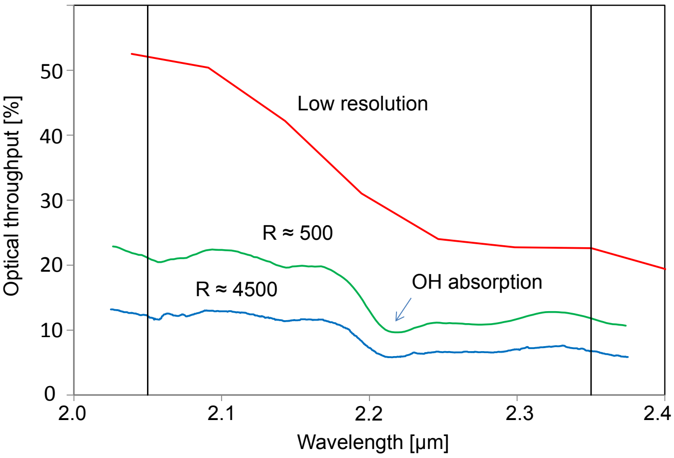

Fig. 7. Optical throughput of the beam combiner instrument – excluding telescopes, VLTI beam relay, and detector quantum efficiency: low (red), $R \approx 500$ (green), and $R \approx 4500$ (blue) spectral resolution. The fringe tracker throughput is comparable to the science spectrometer at low resolution. The lower throughput of the $R \approx 500$ and $R \approx 4500$ spectral resolution is dominated by losses from the grisms.

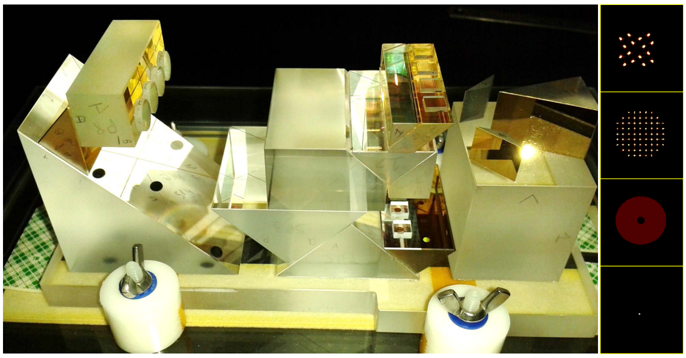

Fig. 8. Acquisition camera beam analyzer: the acquisition and guiding camera provides, for all four telescopes simultaneously, images of the pupil guiding lasers, a Shack-Hartman wavefront sensor, the pupil illumination, and the field (*right*: *top to bottom*, the figure shows only one of the four telescopes). All optical functions are implemented in a single, complex beam-analyzer optics (photograph), located directly in front of the detector. A dichroic beam splitter at the entrance of the beam analyzer redirects the 1200 nm pupil guiding laser to the 2×2 lenslet. H-band light is twice split to image the field for acquisition and guiding, and to feed the Shack-Hartman sensor and pupil viewer.

excluding the detector quantum efficiency for the different spectrometer modes. The average optical throughput of the beam combiner instrument in the 2.05−2.35 μm wavelength range is about 34% when using the low spectral resolution prism. The optical throughputs with the $R \approx 500$ and $R \approx 4500$ grisms are about a factor of two and of four lower (indicative of their respective efficiencies), and on average about 16% and 9%, respectively. The prominent drop in optical throughput at a wavelength of 2.2 μm is mostly due to OH absorption in the silica of the integrated optics (Jocou et al. 2012). The overall quantum efficiency is typically around 0.1−1%, including the losses from telescopes and the VLTI beam relay with a K-band transmission of approximately 30%, the coupling losses into the single-mode fibers from the mismatch between the uniform telescope beam and the fiber's Gaussian mode, the seeing (AT), imperfect adaptive optics correction (UT) and guiding errors resulting in a coupling efficiency of a few % to a few times 10%, and the detector quantum efficiency of 80%.

2.2.7. Acquisition camera and laser guiding system

The acquisition camera (Amorim et al. 2012) provides simultaneously a field image, a pupil image, a Shack-Hartmann wavefront sensor image, and a pupil tracker image for all four telescopes. The H-band (1.45−1.85 μm) field image is used for acquisition and to control low-frequency image drifts. High-frequency image motions from air turbulence in the optical train of the VLTI, which are not seen by the wavefront sensors located in the Coudé rooms of the telescopes, are measured with 658 nm laser beacons launched at the star-separators and detected with position sensitive diodes (Pfuhl et al. 2014). The pupil tracker is a 2×2 Shack-Hartmann-like lenslet in the focal plane and is fed by the 1200 nm pupil guiding lasers launched from the telescope secondary mirror spider arms. This pupil tracker measures both lateral and longitudinal (focus of pupil) pupil motion, and sends corresponding corrections to the instrument internal pupil actuator and the VLTI main delay line variable curvature mirror. The 9×9 Shack-Hartman-sensor is used to focus the ATs, and offers the possibility to measure and correct non-common path aberrations in combination with the UT adaptive optics. All functions of the analyzer optics are implemented through fused silica micro-optics directly in front of the detector (see Fig. 8).

2.2.8. Laser metrology

The GRAVITY metrology (Lippa et al. 2016) measures the differential optical path between the two stars introduced by the VLTI beam relay and the beam combiner instrument. Unlike similar path length metrologies (e.g., PRIMET, Leveque et al. 2003), it does not measure the differential optical path between two telescopes for each star, but measures the differential optical path between the two stars for each telescope. This scheme has the advantage of being largely insensitive to vibrations in the VLTI optical train, and because operated in single path it eases the implementation inside the cryogenic instrument. The metrology receivers are mounted above the telescope primary mirror on the secondary mirror spider arms, which allows for the tracing of all optical elements in the path, and even more importantly, provides a physical and stable realization of the narrow angle astrometric baseline (Woillez & Lacour 2013; Lacour et al. 2014). The metrology laser is a high-power (~1 W), high stability (<30 MHz), linearly polarized continuous wave fiber laser with a wavelength of 1908 nm.

Two low-power beams are injected through the spectrometers into the exit of the integrated optics beam-combiners, and superposed with a third beam launched in free beam from behind the fiber coupler, which serves as an optical amplifier. A direct detection of the interference between the fringe tracker and science metrology laser would require such high power levels in the fibers that the inelastic backscattering from the fluorescence from holmium and thulium contamination and the Raman effect would completely overpower the astronomical signal at wavelengths up to about 2.15 μm. We therefore use the interference with a much brighter third beam, thereby reducing the required flux levels in the fibers, and accordingly reducing the backscattering by an equivalent factor of 1000. The metrology fringe sensing is integrated as a phase-shifting interferometer with lock-in amplifier signal detection between 10 kHz and 20 kHz, with separate frequencies for the fringe tracker and science metrology.

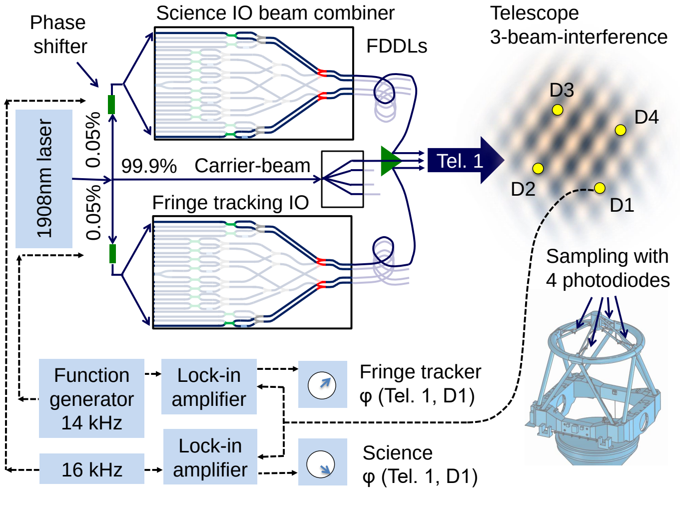

Fig. 9. Laser metrology: schematic shows the working principle of measuring the optical path difference between the two beam combiners and the telescope. The metrology laser is launched from the spectrometers and is detected above the primary mirror at the telescope secondary mirror spider arms. To minimize the laser power in the spectrometer and optical fibers, we do not directly measure the interference between the laser coming from the two beam combiners, but measure separately for the fringe tracker and science beam combiner the phase relative to a very bright, third "carrier" beam. The actual phase measurement is implemented by modulating the phase of the fringe tracker and science metrology at different frequencies, and by measuring the cosine and sine components of the respective interference with the third beam through lock-in amplifiers.

2.2.9. Detectors

The fringe-tracking detector is a Selex (now Leonardo) SAPHIRA 256×320 pixel, near-infrared mercury cadmium telluride (HgCdTe), 2.5 μm cutoff, electronic avalanche photo diode (eAPD) array with a pixel size of 24 μm (Finger et al. 2016). These detectors have been developed in the context of GRAVITY in collaboration with Selex to overcome the noise barrier of complementary metal-oxide-semiconductors (CMOS), which so far has limited the performance of near-infrared sensors at high frame rates of a few hundred Hz. The GRAVITY detectors overcome this noise barrier by avalanche amplification of the photoelectrons inside the pixel. After several development cycles, the eAPD arrays have matured and resulted in the SAPHIRA arrays as used in GRAVITY. The fringe tracker reads twenty-four 32×3 pixel wide stripes at 300 Hz−1 kHz, and uses Fowler sampling with four reads at the beginning and end of the exposure. The fringe-tracking detector is run at a temperature of 95 K. The 2 μm quantum efficiency is about 70% (Finger et al. 2014). The eAPD is operated at a reverse bias voltage of 11.8 V, resulting in an eAPD gain of ~36. The resulting effective read noise is <1 e^- rms, and the excess noise from the amplification process is 1.3.

The science spectrometer and the acquisition camera are each equipped with a Teledyne 2048×2048 pixel, 2.5 μm cutoff wavelength HgCdTe, 18 μm pixel size, HAWAII2RG detector (Finger et al. 2008). The detectors are operated in non-destructive – sampling up the ramp – read mode, using the 32 100 kHz analog outputs. The quantum efficiency at a wavelength of 2 μm is around 80%. The correlated double sampling read noise of the acquisition camera and science spectrometer detectors is 13 e^- and 12 e^- rms, respectively. The effective read noise for sampling with 32 Fowler pairs is about 3 e^- rms. All detectors of GRAVITY are controlled with the ESO New General detector Controller (NGC, Baade et al. 2009).

2.2.10. Calibration unit

The calibration unit (Blind et al. 2014) provides all functions to test and calibrate the beam combiner instrument. It is directly attached to the beam combiner instrument in front of the cryostat and simulates the light from two stars and four telescopes. The artificial stars are fed by halogen lamps or an argon spectral calibration lamp. The calibration unit further provides four motorized delay lines to co-phase the beams, metrology pickup diodes to simulate astrometric observations, linear polarizing filters to align the fiber polarization, tip/tilt and pupil laser beacons for testing the pupil tracker and fast guiding, and rotating phase screens for simulating seeing residuals.

2.2.11. Instrument control software and hardware

The instrument software (Ott et al. 2014; Burtscher et al. 2014) is implemented within the ESO control software framework (Pozna et al. 2008). In addition to the basic instrument control software (ICS), which handles motors, shutters, lamps, and other elements, the instrument software also includes the detector control software (DCS, Cumani et al. 2006), several special devices, field bus devices (Kiekebusch et al. 2014), and various real-time algorithms. The latter are implemented using the ESO tools for advanced control (TAC, Bauvir et al. 2004) and run at a frequency of up to 3.3 kHz. In total, the instrument has more than a hundred devices.

The various control and data acquisition processes are distributed over a total of six Linux workstations (instrument workstation, three detector workstations, workstation for analyzing the fringe tracker residuals and updating the Kalman model, and data recorder workstation), seven VxWorks computers for controlling and commanding the various hardware functions (e.g., motors, piezos, shutters, lamps, and lasers) and real-time applications (metrology, phase sensor, OPD controller, differential delay line controller, and tip/tilt/piston controller), partly connected through a reflective memory ring, and two programmable logic controllers from Beckhoff (stepper motor control) and Siemens (cryo- and vacuum control).

2.2.12. Fringe-tracking

The fringe-tracking system (Menu et al. 2012; Choquet et al. 2014) stabilizes the fringes to allow for long exposures with the science spectrometer, and allows us to operate the instrument close to the white-light condition for accurate phase measurements when doing astrometry. A cascade of real-time and workstation computers (Abuter et al. 2016), connected via a reflective memory ring, analyzes the detector images arriving at 300 Hz to 1 kHz, runs the actual control algorithm, applies it to the actuators, and optimizes the control parameters at runtime.

The first module – the fringe sensor – receives the data stream from the fringe-tracking detector and computes the phase delay and group delay for each of the six baselines. The second module – the OPD controller – then calculates the correction signal for the piston actuators. It also hosts the state machine to switch between fringe search, group delay tracking to center the fringe, and phase-tracking to stabilize the fringe. The fringe tracker is based on a Kalman controller for optimum correction

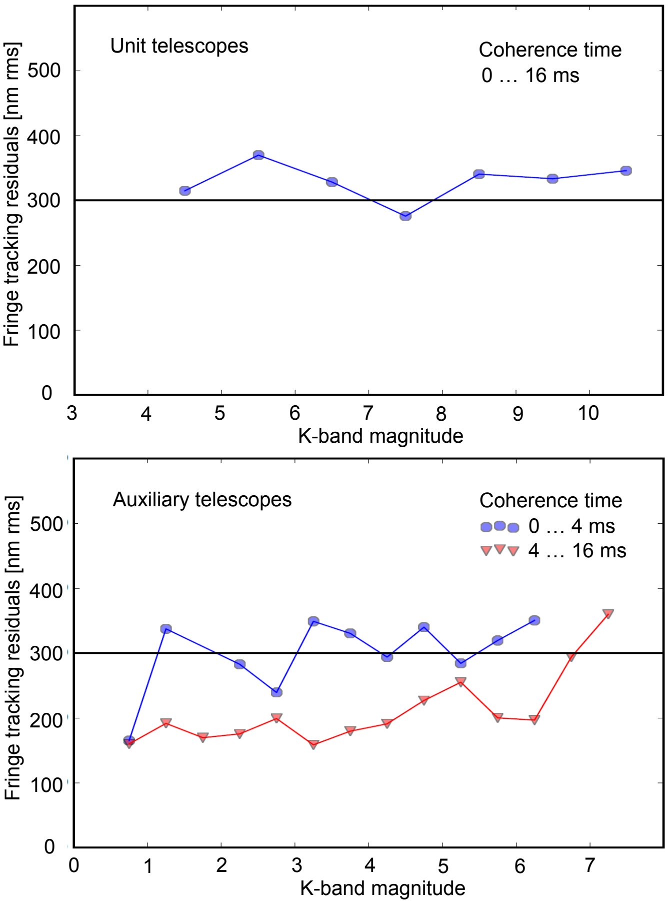

Fig. 10. Fringe-tracking performance: the figures show the fringe-tracking residuals as a function of the reference stars' K-band correlated magnitude for UTs (*top*) and ATs (*bottom*), respectively. The horizontal lines indicate residuals of 300 nm rms, for which the fringe contrast in long exposures is reduced by ~30% in the K-band. For the ATs, we plot the fringe-tracking residuals separately for good seeing with long atmospheric coherence times $\tau_0 > 4$ ms (red), and for short coherence times $\tau_0 < 4$ ms (blue). We do not have enough statistics to make this distinction for the UTs. The OPD residuals for long coherence times are typically 200 nm and 300 nm rms, the limiting magnitudes around $m_K \approx 7$ mag and $m_K \approx 10$ mag for the ATs and UTs, respectively.

of the atmospheric and vibration-induced piston and to mitigate flux dropouts from the fluctuating injection in the fibers. The Kalman model for the piston is an autoregressive model of order 30, the system- and piezo-response is modeled with a fourth order autoregressive model. The Kalman model parameters are automatically updated every few seconds by a non-real-time workstation analyzing the actual OPD residuals and actuator commands. The piston commands from the fringe tracker are finally merged with the laser guiding measurements in a third module – the tip/tilt/piston controller – and applied to the instrument internal tip/tilt/piston piezo actuator. Low frequency OPD variations are offloaded to the VLTI main delay line. The fringe tracker is synchronized with the science detector to sample the science fringes at discrete phase offsets, and to guarantee that 2π phase corrections – resulting from the drift between phase and group delay – are only applied between exposures.

The fringe-tracking performance depends on the atmospheric coherence time τ_0 and the K-band correlated magnitude of the reference star. Figure 10 shows this dependence for the case of on-axis observations, for which the light is equally split between the fringe tracker and science spectrometer. To increase the statistics – especially for the comparably few UT commissioning observations – we have also included off-axis observations by subtracting 0.75 mag from the stars' apparent magnitude. For good observing conditions with an atmospheric coherence time $\tau_0 > 4$ ms, the fringe-tracking limiting magnitude is around $m_K \approx 7$ mag for the ATs and $m_K \approx 10$ mag for the UTs, respectively. The limiting magnitudes for off-axis observations, for which all the light from the reference stars is used for fringe-tracking, are approximately 0.75 mag fainter. The OPD residuals – calculated over a time window of typically a few minutes – are around 200 nm and 300 nm rms, respectively. The larger fringe-tracking residuals for the UTs are caused by uncorrected vibrations of the telescopes and Coudé optics.

2.2.13. Differential delay control

The dOPD between the fringe tracker and science objects is continuously compensated by the instrument internal fiber differential delay lines (Sect. 2.2.3). The differential delay lines are preset using the strain gauge feedback from the piezo actuators; the stabilization is done on the metrology feedback. The dOPD trajectory is calculated in real time from the object coordinates and telescope locations. The typical preset accuracy on the strain gauge is about several 10 μm, the closed loop residuals on the metrology feedback are on nanometer level. The reflective memory ring is used to synchronize the data between the metrology real-time computer and the fiber differential delay controller.

2.2.14. Science fringe centering

The uncertainty in the relative position between the fringe tracker star and the science object, as well as the hysteresis of the fiber delay line and its strain gauge feedback, limits the accuracy of the science fringe centering. The instrument software thus provides the possibility to automatically center the science fringes. This is done in a similar way as with the fringe tracker, but here analyzing the long exposures from the science spectrometer and commanding the differential delay lines.

2.2.15. Field stabilization

The field stabilization is implemented in a three stage control. The atmospheric- and wind-shake-induced image motion is corrected at the telescope level, in the case of the UTs with the GRAVITY CIAO (Sect. 2.3) or MACAO adaptive optics, and for the ATs with the system for tip-tilt removal with avalanche photodiodes (STRAP, Bonaccini et al. 1997) and in the future with the new adaptive optics module for interferometry (NAOMI, Gonté et al. 2016b). When observing with the UTs, the GRAVITY laser guiding system (Sect. 2.2.7) measures the image jitter between the telescope and the beam combiner instrument. This control runs at 3.3 kHz loop rate on a real-time computer, and directly actuates the instrument internal tip/tilt/piston actuator in the fiber coupler (Sect. 2.2.2). The low frequency image drifts are measured by the acquisition and guiding camera with a frame rate of 0.75 Hz. The image analysis (Anugu et al. 2014) and the control are implemented on the instrument workstation. The typical residuals of the acquisition camera guiding are <0.5 pixel (one axis rms), corresponding to <0.2 times the H-band diffraction limit of the telescopes, or <9 milliarcsecond (mas) (UT) and <40 mas (AT).

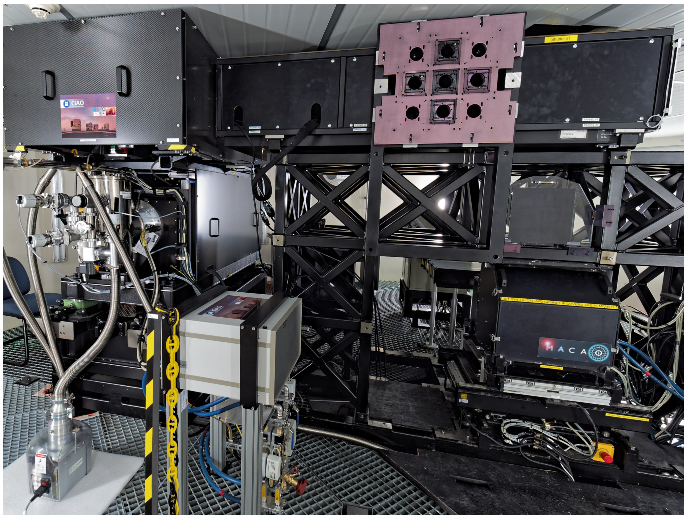

Fig. 11. CIAO: the photograph shows the Coudé room of UT4 in June 2016. The big central structure is the star separator. The CIAO wavefront sensor comprises the tower structure on the left side, with the cryostat connected to a pump on the floor, and the readout electronics located next to it (light gray box connected to blue cooling pipes). The visual wavefront sensor MACAO is located at the lower right.

2.2.16. Pupil control

Accurate lateral and longitudinal pupil control is a prerequisite for narrow angle astrometry (Lacour et al. 2014). The pupil position is traced by the laser beacons launched at the telescope spider arms and measured with the acquisition and guiding camera (Sect. 2.2.7). The image processing (Anugu et al. 2014) and the control loop are implemented on the instrument workstation. The frame rate is 0.75 Hz. The typical accuracy of the lateral pupil guiding is 0.1% (one axis rms) of the pupil diameter, and about 30 mm rms (in the 80 mm diameter collimated beam of the VLTI main delay lines) for the longitudinal pupil guiding.

2.3. Adaptive optics

The GRAVITY CIAO (Scheithauer et al. 2016) is a single conjugated adaptive optics, combining a Shack-Hartmann type wavefront sensor sensitive in the near-infrared $H + K$-bands (1.30–2.45 μm) with the ESO standard platform for adaptive optics real-time applications (SPARTA, Fedrigo et al. 2006), and the bimorph deformable mirror of MACAO (Arsenault et al. 2003).

2.3.1. Wavefront sensor

The CIAO wavefront sensor has 68 active subpupils, with each subpupil corresponding to an area with a diameter of 0.9 m projected on the UT primary mirror. The image scale on the detector is 0.5″/pixel. The instantaneous, unvignetted field of view of the wavefront sensor spans 2″, corresponding to 4 × 4 pixel on the detector. To minimize crosstalk between the subpupils, each subpupil is re-imaged on an 8 × 8 pixel area of the detector. The wavefront sensors use SAPHIRA eAPD detector arrays, which are the same type as used in the fringe tracker, and are described in Sect. 2.2.9. The CIAO wavefront sensors are located in the Coudé room below each of the UTs (see Fig. 11) behind the star separator (Delplancke et al. 2004). The star separator has access to a field of view on sky with a radius of 60″. Within this large field of view, the star separator can select and track two separate beams with a field of view of 2″ each. The star separator also provides actuators for pupil positioning and stabilization. CIAO can pick either of the two star separator outputs, using mirrors to take advantage of all of the light when operated off-axis, or inserting a beam splitter when used on-axis together with the GRAVITY beam combiner instrument. The CIAO beam selector is prepared to host one more beam splitter in preparation for a potential upgrade for use with the future VLTI Multi Aperture Mid-Infrared Spectroscopic Experiment (MATISSE, Lopez et al. 2014). In order to block parasitic light from the 1200 nm GRAVITY pupil beacons and the 1908 nm metrology, the CIAO cryostat (see Fig. 12) entrance window only transmits light in the wavelength range from 1.3–2.45 μm and includes a notch filter blocking light at wavelengths between 1.85 μm and 2.0 μm (Yang et al. 2013).

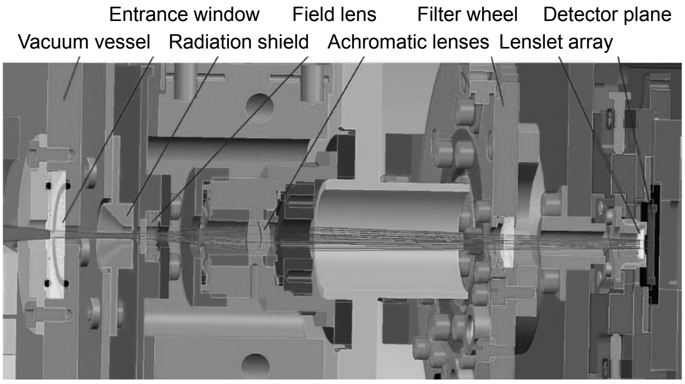

Fig. 12. CIAO cryostat: 3D CAD drawing depicts the CIAO cryostat with its cold optics and actuators. The movable field lens, which is located behind the entrance window, controls the lateral pupil position (Dai et al. 2017) as seen by the lenslet array. The achromatic lenses image the deformable mirror (pupil) onto the lenslet array. The filter wheel houses an $H+K$-band filter, two neutral density filters, a closed position, and an open position.

2.3.2. Target acquisition

For the target acquisition, CIAO scans a field of view of typically 10″ × 10″, automatically identifies the brightest source in this field, and selects the loop frequency and detector gain for optimal performance. The loop frequencies range from 100 Hz (faint star case) to 500 Hz (bright star case). The scanned field of view is displayed to verify the selected reference star, or to manually pick another source, for example, in the case of a crowded field. After closing the adaptive optics loop, CIAO optimizes and stabilizes the pupil alignment using both its internal actuator and the star separator pupil actuator. Once the CIAO acquisition process has been completed, the control is yielded back to the beam combiner instrument for the acquisition of the interferometric targets.

2.3.3. Adaptive optics performance

For bright sources, the adaptive optics performance is limited by the number of actuators (60) of the MACAO deformable mirror. Figure 13 (top) shows the typical K-band Strehl ratio as a function of atmospheric seeing. The Strehl ratio delivered to the VLTI at a seeing of 0.7″ and using a wavefront reference star at a separation of 6″ is 40%. CIAO fulfills or outperforms all its top-level requirements (Deen et al. 2016), in particular for the on-axis K-band Strehl ratio of ≥35% and ≥10% on stars

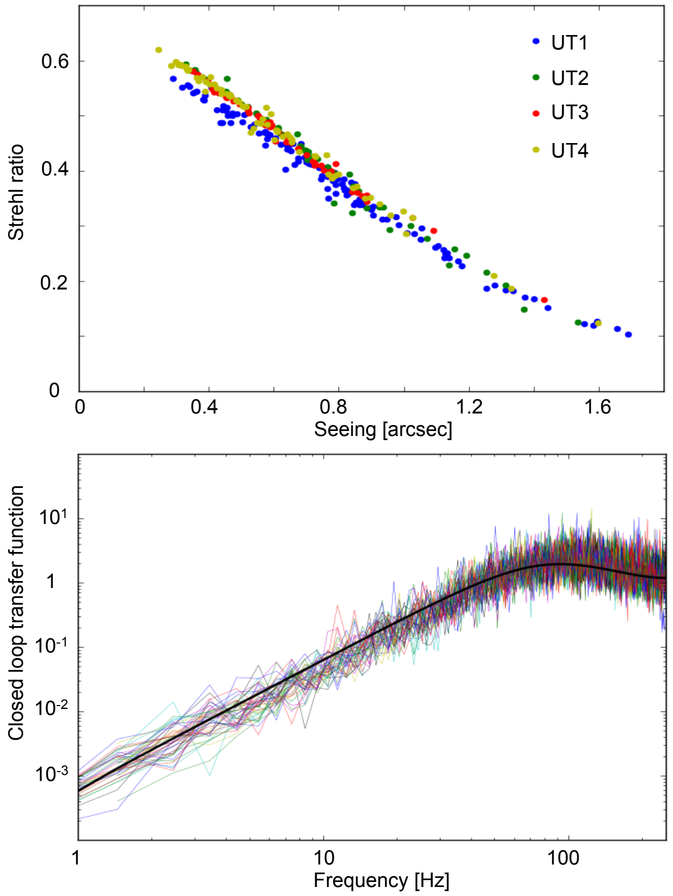

Fig. 13. Adaptive optics performance: the *top panel* shows the K-band Strehl ratio as a function of atmospheric seeing (at 500 nm). The Strehl ratio and seeing are derived from the wavefront residuals as observed with the wavefront sensor, and calibrated with K-band observations of the components of wide binary stars using the VLTI Infrared Image Sensor (IRIS, Gitton et al. 2004). The *bottom panel* shows the closed loop transfer function for Zernike modes up to order 44 as measured on the $m_K = 6.5$ mag star GC IRS 7. Both curves are representative for observations of bright objects with $m_K \lesssim 7$ mag.

with $m_K = 7$ mag and $m_K = 10$ mag, respectively[3]. Figure 13 (bottom) shows the closed loop transfer function obtained on GC IRS 7, the wavefront reference star for the observations of the Galactic center (Sect. 3.5). In better than average observing conditions, CIAO works on guide stars as faint as $m_K \approx 11$ mag. It provides better performance than the visible MACAO on objects with $V - K \geq 4.5$ mag. CIAO also includes neutral density filters for observations of bright stars.

2.4. Data reduction software

The data reduction software provides all routines for the calibration and reduction of the data collected with the instrument. It covers routines for the instrument calibration, single beam observations, and dual-beam observations. The inputs are the science combiner detector frames, the fringe tracker frames, the metrology signals from the diodes in the fiber coupler and at the telescopes, and the images from the acquisition camera. The outputs of the data reduction software are calibrated complex visibilities, reconstructed quick-look images, and astrometry data.

The main data reduction algorithm of the GRAVITY pipeline is based on the principle of the pixel to visibility matrix (P2VM, Tatulli et al. 2007). The P2VM characterizes the photometry, coherence, and phase relations between the four inputs of the integrated optics components and their 24 outputs (six baselines times four outputs). An overall description of the algorithms used in GRAVITY is given in Lapeyrere et al. (2014). A complete instrument calibration data set includes the P2VMs of the two beam combiners, the map of the spectral profiles of the science spectrometer, the wavelength calibration of the fringe tracker and science spectrometer, as well as dark frames and bad pixel maps. These calibration data are computed from a series of raw files collected using the calibration unit. The wavelength scale is also derived from this sequence, using the metrology laser wavelength as the fiducial reference. The properties of the interference fringes (photometric spectra, complex visibilities, closure quantities) as a function of wavelength are computed separately for the fringe tracker and science beam combiners. In addition, when used in dual field mode, GRAVITY provides the phase of the science fringes referenced to the fringe tracker, which can be translated into an astrometric separation vector. Optionally, the pipeline can also analyze the acquisition camera frames.

The data reduction software code is written in standard ANSI C using ESO's Common Pipeline Library (McKay et al. 2004). It is made available through ESO. The MiRA image reconstruction algorithm (Thiébaut 2008, 2013) is interfaced with the GRAVITY pipeline through a dedicated processing recipe and is included in the data reduction software distribution. The GRAVITY pipeline can be executed using the `esorex` command line tool, from the `Gasgano` graphical user interface (ESO 2012), or from a `reflex` graphical workflow (Ballester et al. 2014). Alternatively, a set of `python_tools` developed by the GRAVITY consortium can be used to run the reduction, calibrate, and visualize the raw and processed data.

The output files produced by the data reduction software follow the Optical Interferometry FITS version 2 standard (Duvert et al. 2016). They can therefore be visualized and analyzed using standard interferometric software packages such as offered by the Jean-Marie Mariotti Center, with interferometric image reconstruction codes (see, e.g., Monnier et al. 2014, for a review of existing codes), and special analysis software such as, for example, the companion analysis and non-detection in interferometric data tool CANDID (Gallenne et al. 2015).

2.5. Measurement precision

The precision of the interferometric phase and visibility amplitude in long science exposures is a function of the source brightness and the fringe-tracking residuals. The standard deviations of these quantities are calculated by the data reduction software (see Sect. 2.4) by bootstrapping[4] the measurements from the individual exposures of each data set. Figure 14 shows the histograms of the standard deviations of the visibility phase and amplitude for bright calibrator stars observed with the ATs in good conditions, with fringe-tracking residuals smaller than 300 nm rms. The fringe-tracker was run at a frame rate of 909 Hz and a closed-loop cutoff frequency of around 60 Hz (Abuter et al. 2016). The data represented in the histograms are

---

[3] At a zenith distance of 30° for the standard Paranal atmosphere with zenith seeing of 0.85″ (corresponding to $r_0 = 0.12$ m), coherence time of 3 ms, and (zenith) isoplanatic angle of ~2″ at a reference wavelength of 500 nm.

[4] See, for example, Sect. 15.6 of Press et al. (2002) for an introduction to the bootstrap method.

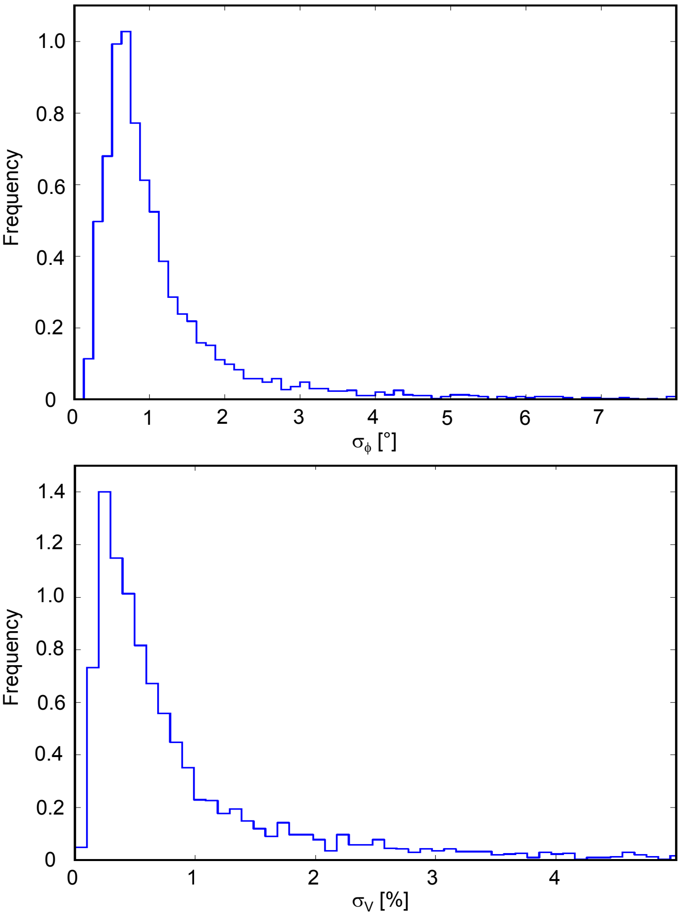

Fig. 14. Measurement precision: the figures show the histograms of the wavelength-averaged standard deviations of the visibility phase σ_Φ (*top*) and amplitude σ_V (*bottom*) for the observation of bright calibrator stars. They typically peak around 1° and 0.5%, respectively.

the wavelength-averaged uncertainties for each baseline and data set. We analyzed around 600 data sets. Each data set typically contains 30 exposures with individual integration times between 0.3−30 s. The precision of the visibility amplitude is about 0.5%, and about 1° for the visibility phase. The results for the UTs are similar to the ATs.

3. First GRAVITY observations

This section illustrates the observing modes and demonstrates the performance of GRAVITY for several archetypical objects observed during commissioning and early guaranteed time observations.

3.1. High accuracy visibility observations of resolved stars

The fidelity of interferometric imaging relies on high accuracy visibilities and phases. The dynamic range – the intensity ratio of the brightest and faintest objects detectable in the image – is to first order inversely proportional to the noise in the visibility and phases. Also imaging resolved stars with their low contrast surface features requires a very high visibility accuracy (e.g., Haubois et al. 2009). We demonstrate the exquisite accuracy of GRAVITY and its visibility calibration with two examples among the best we have obtained so far, the observations of ξ Tel (Sect. 3.1.1) and 24 Cap (Sect. 3.1.2). They are examples for the two regimes of high and very low visibilities, respectively. We took the data in medium spectral resolution ($R \approx 500$) on the nights of 7 and 8 October 2016 with the ATs in the A0-G1-J2-K0 configuration.

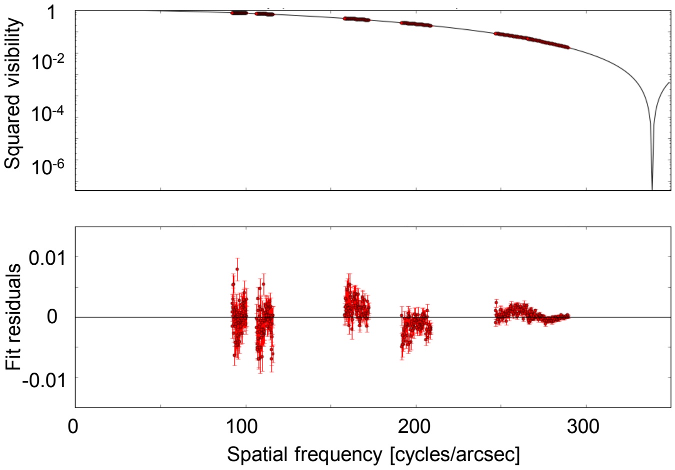

Fig. 15. Limb darkening in the K5 III giant ξ Tel: the *top panel* shows the observed squared visibility for ξ Tel. The solid line is the best fit limb darkening disk model. The fit residuals (*bottom*) are typically smaller than 0.005, corresponding to a visibility accuracy of better than 0.25%.

3.1.1. Limb darkening in ξ Tel

We measured the accuracy of GRAVITY at high visibilities with the K5 III giant ξ Tel, a bright $m_K = 0.91$ mag star (Fig. 15). Each calibrated point is the combination of 30 exposures of 5 s each. We calibrated the visibilities against the observation of HD 184349, a $m_K = 3.47$ mag unresolved K4 giant star (K-band diameter of 1.09 ± 0.05 mas following Perrin et al. 1998). The fit for the 2.10−2.29 μm wavelength range with a uniform disk visibility function yields a diameter of 3.6491 ± 0.0007 mas with a reduced $\chi^2 = 9.9$, and is thus unsatisfactory. A much better fit with a reduced $\chi^2 = 2.8$ is obtained with a single power law limb darkening disk model from Hestroffer (1997). It gives a diameter of 3.881 ± 0.007 mas and a mean limb darkening exponent of 0.45 ± 0.01. The squared visibility residuals are presented in the bottom panel of Fig. 15. They are typically smaller than 0.005, corresponding to less than 0.25% on the visibility. The limb-darkened disk model reduced the residuals by a factor of two compared to the uniform disk. Even though the star is not fully resolved, the GRAVITY data are clearly accurate enough to detect limb darkening in the first lobe of the visibility function.

3.1.2. Depth of the first null of 24 Cap

We measured the accuracy of GRAVITY at low visibilities with the K5/M0 III giant 24 Cap, a bright $m_K = 0.53$ mag star (Fig. 16). Each calibrated point is the combination of 30 exposures of 5 s each. As a visibility calibrator star we used HD 196387, a $m_K = 3.47$ mag unresolved K4 giant star (K-band diameter estimated to 1.093 ± 0.015 mas by Mérand et al. 2005). Because of the high brightness of the source, the fringe tracker detector response was nonlinear by a few percent. The resulting additive errors are larger when the visibilities are high, therefore primarily affecting the low spatial frequency channels, whose visibilities get underestimated. We thus excluded the visibilities of the shortest baseline from the model fitting, and applied an

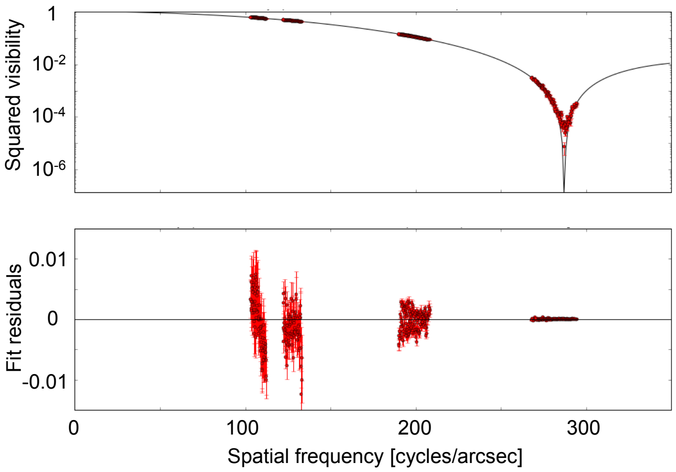

Fig. 16. Depth of the first null of the K5/M0 III giant 24 Cap: the *top panel* shows the observed squared visibility for 24 Cap. The depth of the null of the first minimum is 8×10^{-6}, corresponding to a visibility modulus of 0.3%. The non-zero visibility is likely caused by the granulation in the star's surface. The solid line is the best fit limb darkening disk model, the fit results are shown in the *lower panel.*

ad-hoc correction by a factor 1.025 in Fig. 16. We fitted the data with a single power law limb darkening disk model from Hestroffer (1997) over the 2.10−2.29 μm wavelength range. This gives a diameter of 4.473 ± 0.005 mas and a mean limb darkening exponent of 0.304 ± 0.008. The squared visibility residuals are presented in the lower panel of Fig. 16. They are typically smaller than 0.01 (equivalent to residuals less than 0.5% on the visibility at high visibility).

The spatial frequency coverage allowed us to sample the first zero of the visibility function and to measure the depth of the first null. As shown on the upper panel of Fig. 16, the minimum squared visibility is 8×10^{-6} or a visibility modulus of 0.3%. This is comparable to measurements of other K giants with high accuracy instruments, for example, the measurement of Arcturus, another K giant, with the Integrated Optics Combiner (IONIC) at the Infrared-Optical Telescope Array (IOTA) by Lacour et al. (2008). The typical value of a few 0.1% for the null depth is probably of astrophysical origin and explained by the granulation at the surface of the star. GRAVITY is therefore at least as good as the most accurate interferometers to remove biases on squared visibilities.

3.2. Spectro-differential visibilities of the T Tauri binary S CrA

The physical structure and processes in the inner regions of protoplanetary disks are still poorly constrained, yet they are key for understanding planet formation. In this region, accretion flows, winds, and outflows are essential to control angular momentum, alter the gas content, drive the dynamics of the gas, and set the initial conditions for forming terrestrial planets. The observations of the innermost few astronomical units require milliarcsecond resolution as provided by infrared interferometry. Anthonioz et al. (2015) and Lazareff et al. (2017) have presented broad-band interferometric surveys of T Tauri and Herbig AeBe stars, respectively, to derive the statistical properties of the dust distribution in the inner disks. GRAVITY will be able to take the next steps and image the hot (Brγ) and warm (CO) gas in the protoplanetary disks, as well as to extend the sample to a wider range of stellar masses, ages, and disk properties.

As an illustration, we used the dual-field mode of GRAVITY to perform spectro-differential interferometry on the T Tauri binary system S CrA, which consists of an early G-type primary and an early K-type secondary star. These are the first high spectral resolution $R \approx 4500$ interferometric observations of a T Tauri star. The star S CrA North, for example, was observed with the VLTI before (Vural et al. 2012), but it was out of reach for the spectro-interferometric resolution of its spectral lines. The binary S CrA is particularly well suited for GRAVITY observations with the UTs, because its separation of about 1.3″ allows us to use the dual-field mode, thereby avoiding splitting the light between the fringe tracker and the science spectrometer, and increasing the sensitivity by a factor of two. The star S CrA North has a brightness of $m_K = 6.6$ mag and the star S CrA South has a brightness of $m_K = 7.3$ mag (Prato et al. 2003). Both stars were observed at high spectral resolution on 19 July 2016 and 15 August 2016 with the four UTs. On both nights we swapped between the two components of the binary system, that is, we first used the southern component for fringe-tracking to observe S CrA North at high spectral resolution and with long integration times, and subsequently swapped the two stars to fringe-track on S CrA North and to perform long integrations on S CrA South. Each measurement consists of five exposures with 60 s integration time. We calibrated each visibility point with on-axis observations of HD 188787.

Figure 17 shows the observed spectrum, visibilities, and differential phases of S CrA North around the hydrogen Brγ line. We calibrated the absolute visibility of the continuum using the fringe tracker data recorded as part of the swapping sequence. From the Gaussian fit to the K-band visibilities, we find a half-flux radius for the continuum emission around the Brγ line of 0.83 ± 0.04 mas, which translates to 0.108 ± 0.005 AU at a distance of 130 pc (Prato et al. 2003). The Brγ emission line of S CrA North is double-peaked at 2.1635 μm and 2.1661 μm, corresponding to radial velocities of about $-360\,\mathrm{km\,s^{-1}}$ and $0\,\mathrm{km\,s^{-1}}$, respectively. For all six baselines, the visibility increases around the peak of the line. On the other hand, the visibilities across the Brγ emission line vary between the baselines, and a phase signal of few degrees is only detectable on three baselines. Our observations therefore suggest the presence of two structures in the environment of S CrA North with different kinematic signatures at small and large scales. Thanks to spectro-differential interferometry, GRAVITY thus provides new insights into the innermost regions of T Tauri stars, probing the complex accretion-ejection phenomena at play.

3.3. Imaging the core of η Car

The relative proximity of η Car makes it one of the best observable high-mass stars in the Galaxy. GRAVITY enables spectrally resolved interferometric imaging of the central wind region of this compact binary. At an apparent brightness of $m_K = 0.94$ mag, this target is bright enough for observations with the ATs, which can be relocated to different configurations and thereby provide the rich baseline coverage needed for high fidelity interferometric imaging. We observed η Car at high-spectral resolution ($R \approx 4500$) and split-polarization on 25 and 28 February 2016, and obtained ten data sets with the A0-G1-J2-K0 telescope configuration, plus four more data sets with the A0-G2-J2-J3 configuration. Each data set consists of 30 exposures with 10 s integration time. The top left panel of Fig. 18 displays the baseline coverage of the observations. With a maximum baseline B of ~130 m and minimum baselines of ~40 m, we obtain angular resolutions $\theta = \lambda/2B \approx 1.7{-}5.6$ mas at the

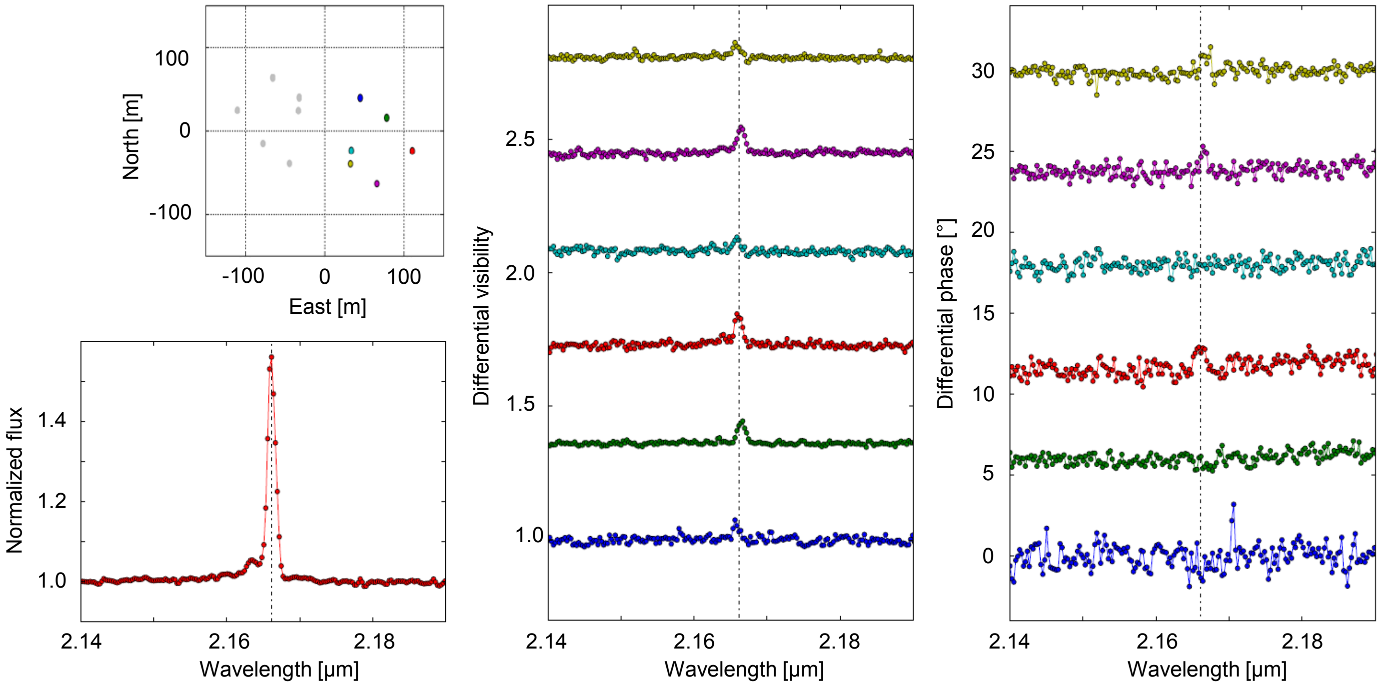

Fig. 17. Spectro-differential interferometry of the T Tauri star S CrA North: the *lower left panel* shows the spectrum around the double-peaked hydrogen Brγ emission line. The *middle and right panels* display the observed differential visibilities and phases, respectively, for the six UT baselines depicted on the *top left*. The asymmetry and velocity offsets in the visibilities of the Brγ line at short baselines and the more symmetric visibility spectrum at long baselines point towards two different structures in the ionized gas of the innermost accretion and ejection region of T Tauri stars.

wavelength of Brγ, respectively. The squared visibilities have an average signal-to-noise ratio of 23 and the closure phases exhibit an average error of 5.5°. The calibrated spectrum (top right panel of Fig. 18) contains several lines, the most prominent corresponding to He I 2s−2p (2.059 μm) and Brγ (2.166 μm).

The high accuracy visibilities (see 3.1) and the high signal-to-noise ratio allow a chromatic image reconstruction of η Car across the Brγ line. For this we used SQUEEZE (Baron et al. 2010), an interferometry imaging software that allows for the simultaneous fitting of the squared visibilities, closure phases, and chromatic differential phases. Compared to radio interferometric observations, the few telescopes combined in optical interferometry provide only a sparse baseline coverage, and the image reconstruction is usually guided with so-called regularizers. In our case we used a combination of the L0-norm to avoid spurious point-like sources and a Laplacian to enhance the extended structure expected in some channels. In addition we included a spectral regularizer that computes the L2-norm across the different spectral channels to ensure spectral continuity across the emission line. SQUEEZE uses a simulated annealing Monte-Carlo algorithm as the engine for the reconstruction. In our case, we created 30 chains with 250 iterations each to find the most probable image. We used a 167×167 pixel grid with a scale of 0.6 mas/pixel, and chose a Gaussian with 50% of the total flux centered in the image as the starting point for the reconstruction. The final images are the average of the frames from the different Monte-Carlo chains that converged to a reduced $\chi^2 \sim 1$. The bottom panels of Fig. 18 display eight images across the Brγ line, each convolved with a Gaussian with a full-width-half-maximum (FWHM) of 1.76 mas.

The reconstructed images reveal the different wind components of η Car. The first and last frames, close to the continuum level, show a compact structure with a size of ~5 mas. This compact component is the optically-thick primary wind reported previously with interferometric observations (van Boekel et al. 2003; Weigelt et al. 2006). It is slightly elongated with a position angle of ~134°, which is coincident with the orientation of the major-axis of the homunculus (position angle ~131°). The cavity created by the wind-wind collision between the two binary components (Madura et al. 2013) is seen at a velocity of ~−275 km s^{-1}. At this velocity, η Car shows an asymmetric elongated structure with a size of ~15 mas, with a major axis in the south-east direction. This result is consistent with the fan-shaped morphology found by Weigelt et al. (2016) for similar velocities using the Astronomical Multi-Beam Combiner (AMBER, Petrov et al. 2007) at the VLTI. The morphology of the Brγ blue wing could be also affected by an additional contribution from the fossil winds at the core of η Car (Gull et al. 2011, 2016). In contrast, the red wind exhibits a more compact structure, because the emitting region corresponds mainly to the back side of the primary wind. As illustrated by this example, the spectro-interferometric capabilities of GRAVITY, combined with its high-sensitivity and performance, provide unique tools for chromatic image reconstruction to reveal the milliarcsecond morphology of a large variety of astrophysical targets.

3.4. *Microarcsec spectro-differential astrometry*

In the examples of resolved stars (Sect. 3.1), we have concentrated on the absolute accuracy of the visibility modulus. When it comes to position measurements, however, the information is better traced by the interferometric phase. For example, a phase difference of 1° at a wavelength of 2.2 μm and a baseline of 130 m corresponds to an angular displacement of 10 μas. This kind of accuracy is easily achieved by GRAVITY when looking at the phase difference over a narrow wavelength range. In

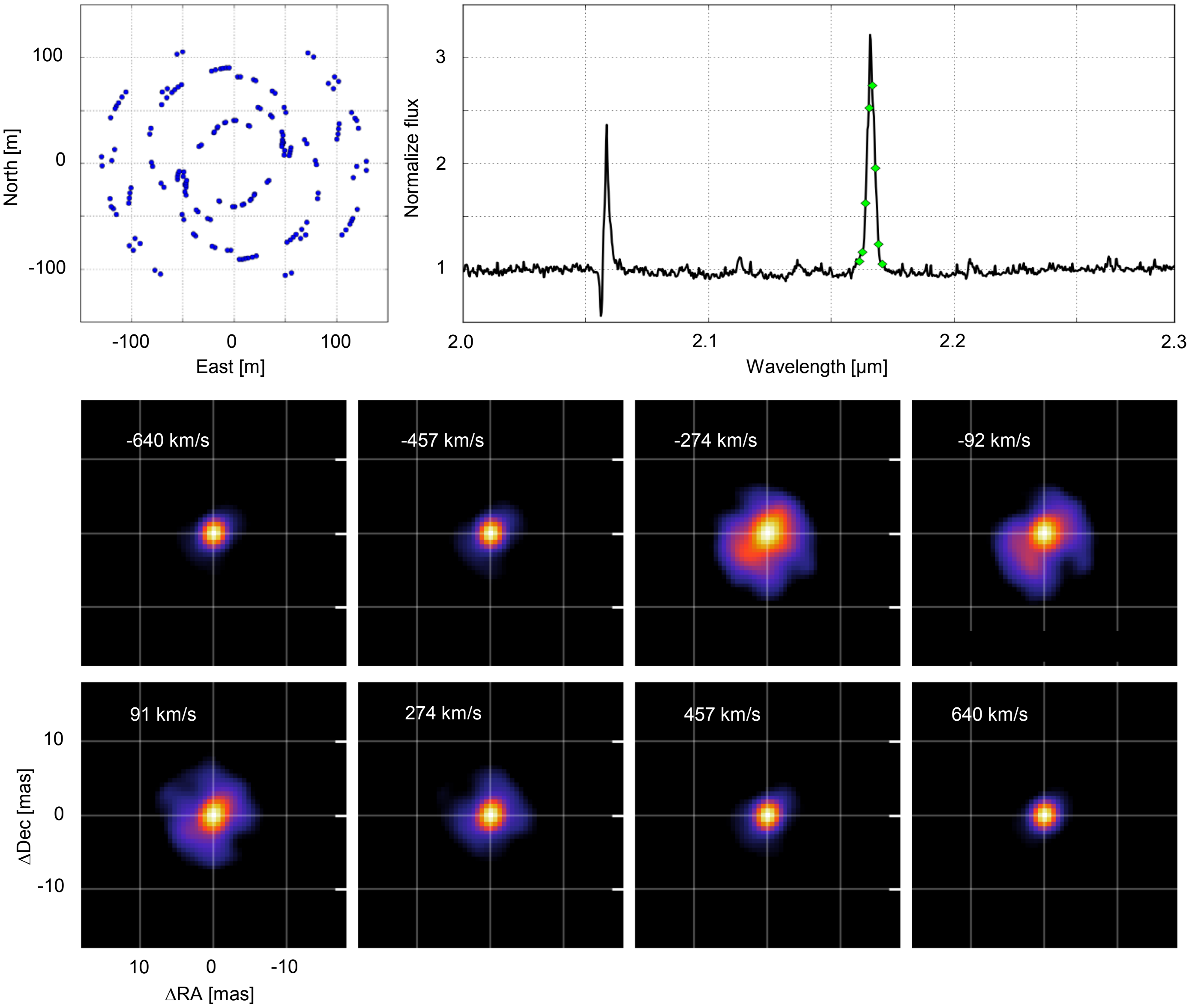

Fig. 18. Core of η Car at mas resolution: the *top left panel* displays the baseline coverage of our observations with the ATs. The *top right panel* shows the observed spectrum around the He I and Brγ emission lines. The *lower panels* present the reconstructed images for different wavelengths (indicated by the green diamonds in the spectrum) across the Brγ line. The frames are individually normalized, the minimum brightness corresponds always to 5% of the maximum brightness. The images reveal the complex morphology of the primary wind and its interaction with the wind from the hidden secondary star.

the following we demonstrate such 10 μas spectro-differential astrometry on the examples of tracing the wind or gas stream in the high-mass X-ray binary (HMXB) BP Cru and the broad line region of the quasar PDS 456.

3.4.1. Tracing the inner region of the HMXB BP Cru

With typical orbital size scales <1 mas, X-ray binaries are beyond the imaging resolution of optical/near-infrared interferometers. As a result, spatial information about the accretion and outflow processes or binary interaction is typically inferred from photometry and spectroscopy. For systems containing spectral lines, however, spectro-differential interferometry may be used to achieve differential astrometry on the few μas scale between continuum and line emission. This technique builds on the exquisite differential visibility and phase precision which GRAVITY achieves by virtue of its fringe tracker and the possibility for minute long coherent integrations at high spectral resolution. To demonstrate this techniques, we have observed the HMXB stars SS 433 (GRAVITY Collaboration et al. 2017a) and BP Cru (GRAVITY Collaboration et al. 2017b) as part of the GRAVITY commissioning.

Here we give the example of BP Cru. The observation were done on the night 18 May 2016 using the four UTs. The total on-source integration time was 2100 s with individual exposures of 30 s. We took all data in high spectral resolution ($R \approx 4500$). The binary BP Cru is a canonical HMXB, in which the massive ($>1.85\,M_\odot$), slowly rotating ($P = 696$ s) pulsar GX 301-2 accretes from the strong stellar wind of the early-blue hypergiant Wray 977 (Kaper et al. 2006) along an eccentric orbit ($e = 0.462$). X-ray lightcurves and column densities, however, show evidence of a more complex accretion mechanism, which likely includes a gas stream of enhanced density (Haberl 1991; Leahy & Kostka 2008). Furthermore, X-ray photoionization and

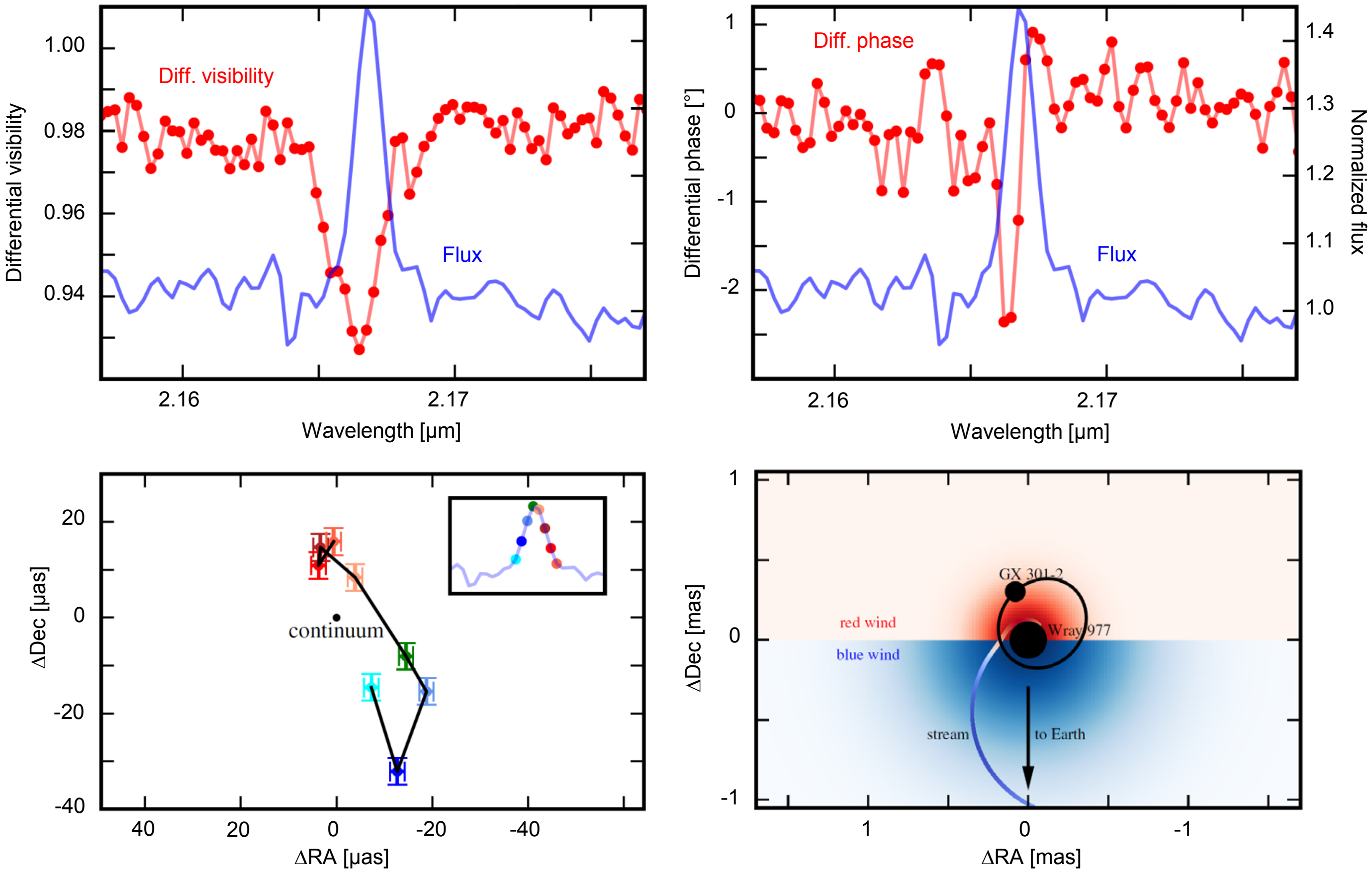

Fig. 19. Tracing the inner region of the HMXB BP Cru: the *top* figures display the differential visibility amplitudes (*left*) and phases (*right*) across the Brγ line (red) and the continuum normalized spectrum (blue) exemplary for one of the six observed baselines. The *lower left panel* shows the model-independent centroid positions for each wavelength across the Brγ line. The image on the blue side of the line has a larger centroid shift than the image on the red side. We note the μas scale on the *lower left panel*. The schematic on the lower right panel shows the BP Cru system as inferred from simple geometric model fits to the interferometric signatures. The donor star, the X-ray pulsar, and its binary orbit are shown in black. An extended wind could explain the visibility amplitude drops across the emission line. A size asymmetry between the blue and red shifted sides of the wind could be related to the X-ray illumination by the compact object. Non-zero visibility phases, also asymmetric between blue and red wavelengths, could be explained by the presence of a gas stream. A simple stream model following Leahy & Kostka (2008) is shown in the bottom right, with the colors along the stream corresponding to the radial velocity measured at Earth ($i = 60°$).

heating could substantially affect the side of the stellar wind facing the pulsar (Blondin 1994; Čechura & Hadrava 2015). Therefore spatially resolving the inner region of this system could provide important information about the gravitational and radiation effects of the compact object on the stellar companion.

The K-band spectrum of BP Cru obtained with GRAVITY shows prominent emission lines of He I (2.059 μm) and Brγ (2.166 μm), both of which show differential visibility amplitudes and phase signatures across the line. Figure 19 shows the example of the Brγ line for the UT1-UT4 baseline. We note the typical standard deviation in the continuum is ~0.4% and ~0.2° for amplitudes and phases, respectively, the latter of which corresponds to 2 μas for a 100 m baseline. These signatures can be used in the framework of the marginally resolved limit (Lachaume 2003) to derive model-independent information about the moments of the flux distribution. They point to velocity dependent centroids and extension across the line, which cannot be explained by a symmetrical, undisturbed stellar wind. Figure 19 (bottom) shows the centroids of the image in the sky plane as a function of wavelength across the line. The blue side must be more displaced from the continuum than the red side, and they are in opposite directions.

The fitting of simple geometrical models suggests an extended, distorted wind observed on scales a few times the size of the orbit. Alternatively the differential phases could be explained by a compact, linear structure with orbital size scale, potentially associated with a gas stream from the donor star. Future spectroscopic observations at high resolution, coupled with interferometric observations at different orbital phases, will help to distinguish between more complex models.

3.4.2. Broad line region of the quasar PDS 456

What is the degree of ordered versus virial motion of the broad line region (BLR) in active galactic nuclei (AGN)? The answer is key to improving the mass-luminosity and size-luminosity relations of AGN, which in turn are cornerstones for using quasars as cosmological standard beacons and to trace the co-evolution of massive black holes and their host galaxies. If the degree of ordered rotation is high, this rotation should be reflected in a velocity dependent displacement of the order of a few 10 μas for the brightest AGN (Rakshit et al. 2015).

The astrometric signature is expected to be particularly large for the strong Paα line, but this line is only observable in K-band for a redshift larger than $z \gtrsim 0.07$. We thus selected the

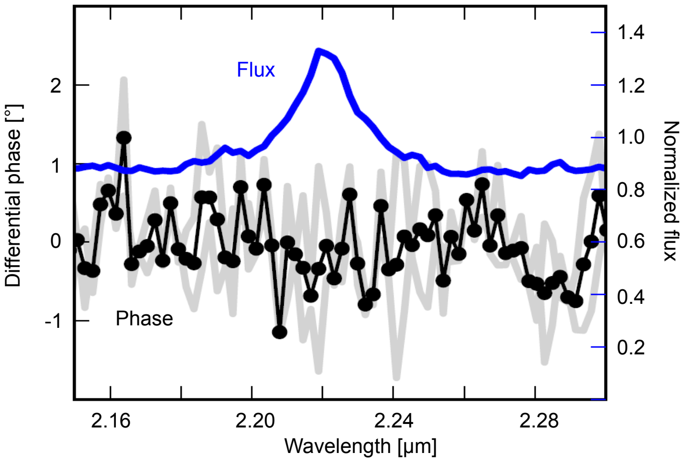

Fig. 20. Broad line region of the quasar PDS 456: the plot shows the normalized spectrum (blue) and differential phase (black) of the broad Paα line for the average of the UT1-UT4 and UT2-UT4 baselines (individual baselines in light gray). No differential phase signature is detected, neither in the individual baselines nor in their average, despite a precision of $\lesssim 1°$.

quasar PDS 456 ($m_K = 9.9$ mag, $m_V = 14.0$ mag), a $z = 0.184$ near-Eddington X-ray source (Reeves et al. 2000), to observe with GRAVITY and the UTs using the visible adaptive optics MACAO on 19 July 2016. We used the medium spectral resolution ($R \approx 500$) with exposure times of 30 s per frame, and spent a total of 3900 s on source. We detected significant coherent flux on all baselines, despite problems with the fringe-tracking because of the limited MACAO performance at faint V magnitudes. The continuum appears partially resolved, with a best Gaussian fit FWHM size of ~0.3 mas, comparable to the angular size expected from the relation between dust sublimation radius and AGN luminosity (Netzer 2015). This size is much smaller than the VLTI beam and subject to systematic errors in calibration, and so we cautiously interpret it as an upper limit of 0.6 mas.

Figure 20 shows the observed spectrum and differential phase. The broad Paα line – redshifted to the K-band – has a FWHM of 3200 km s^{-1}. No differential phase or amplitude signature is detected at the Paα line, despite a precision of $\lesssim 1°$ on each of the two longest baselines. This constrains the line centroid displacement to $\lesssim 10\,\mu$as. Using the measured line strength and assuming ordered rotation or outflow, we place an upper limit on the offset of the line emission from the continuum of $\lesssim 150\,\mu$as. Assuming the broad line is produced at the same spatial scale as the continuum emission, $\lesssim 50\%$ of the line flux could be produced by a component with ordered velocities. Given the phase noise demonstrated by these observations, future GRAVITY observations should be able to probe the structure of the broad line regions of many AGN (e.g., Rakshit et al. 2015).

3.5. GRAVITY observations of the Galactic center

The main scientific driver for GRAVITY is the supermassive black hole in the Galactic center (e.g., Genzel et al. 2010, and references therein), and addresses several fundamental questions in physics and astrophysics. These include: does Einstein's theory of general relativity correctly describe the dynamics and light propagation in its vicinity? What is the exact mass and what is the spin of the black hole? Do the stars follow simple general-relativistic orbits around a single central mass, or are the effects from encounters with dark objects or from an extended mass distribution stronger than the general relativistic effects? How do black holes accrete, and which physics is at work in the inner accretion and outflow region? Is there a jet ejected from the black hole? The GRAVITY collaboration will spend the largest fraction of its guaranteed observing time with the UTs to tackle these questions.

3.5.1. Observing strategy and first observations

GRAVITY employs two main observing modes on the Galactic center. First, interferometric imaging of the central region to (a) precisely measure the orbital parameters of the star S2 relative to the black hole, during the years when S2 is closest to Sgr A* and both are within the same interferometric field of view, to (b) trace the motion of flares on short timescales, which is expected if the emission originates from a small region on a close orbit or in a jet, and to (c) search for fainter stars in the central light week and follow their short period orbits. The second observing mode is long-term astrometric monitoring of the S-stars and the flaring black hole relative to more distant reference stars on very long period orbits. These data would also characterize the binary nature and winds of the reference stars, which are members of the population of young massive stars in the Galactic center. Both types of observation can be executed simultaneously thanks to the dual-beam design of GRAVITY.

Here we report on our first Galactic center observations with the full GRAVITY instrument on 20 and 21 September 2016, shortly after the installation of all four CIAO systems[5]. The atmospheric conditions were slightly better than the median with an optical seeing ~0.7″ and a coherence time of 4 to 5 ms. We used the bright supergiant GC IRS 7 ($m_K \approx 6.5$ mag), located 5.5″ north of Sgr A* for the wavefront sensing with CIAO. The observing sequence was as follows: first we used the brightest WR/O star in the field, GC IRS 16NE ($m_K = 8.9$ mag, Paumard et al. 2006), for fringe-tracking and observed GC IRS 16C ($m_K = 9.7$ mag) with the science beam combiner in low resolution mode ($R \approx 22$). Then we swapped the two stars, that is, we used GC IRS 16C for fringe-tracking and observed GC IRS 16NE with the science beam combiner. This swapping provides an efficient cross-calibration of the visibilities and at the same time gives the astrometric zero point for the laser metrology. After the swapping sequence, we fed S2 to the science beam combiner, while GC IRS 16C remained the fringe-tracking star. On 21 September 2016 we extended the observing sequence with a blind offset to the position of Sgr A*. We noticed a moderately bright flare from Sgr A* on the acquisition camera and decided to stay on the object until we reached the compensation limit of the VLTI delay lines. After that we observed the sky frames.

3.5.2. No stars brighter than $m_K = 17.1$ mag near S2

The star S2 is one of the stars with the closest known peri-center distance to Sgr A*. It orbits Sgr A* with a period of 16 years (Schödel et al. 2002; Ghez et al. 2008; Gillessen et al. 2017) and reaches a velocity of up to 7600 km s^{-1}, that is, 2.5% the speed of light, which makes it a prime candidate to study general relativistic orbit effects close to a supermassive black hole. At an apparent magnitude of $m_K = 14.1$ mag, S2 was far too faint

---

[5] We obtained first fringes of S2 already on 18 May 2016. See `https://www.eso.org/public/news/eso1622/`. At that time our CIAO infrared wavefront sensors were not yet fully installed, and we took advantage of exceptionally good seeing conditions, using the visible light wavefront sensor MACAO.

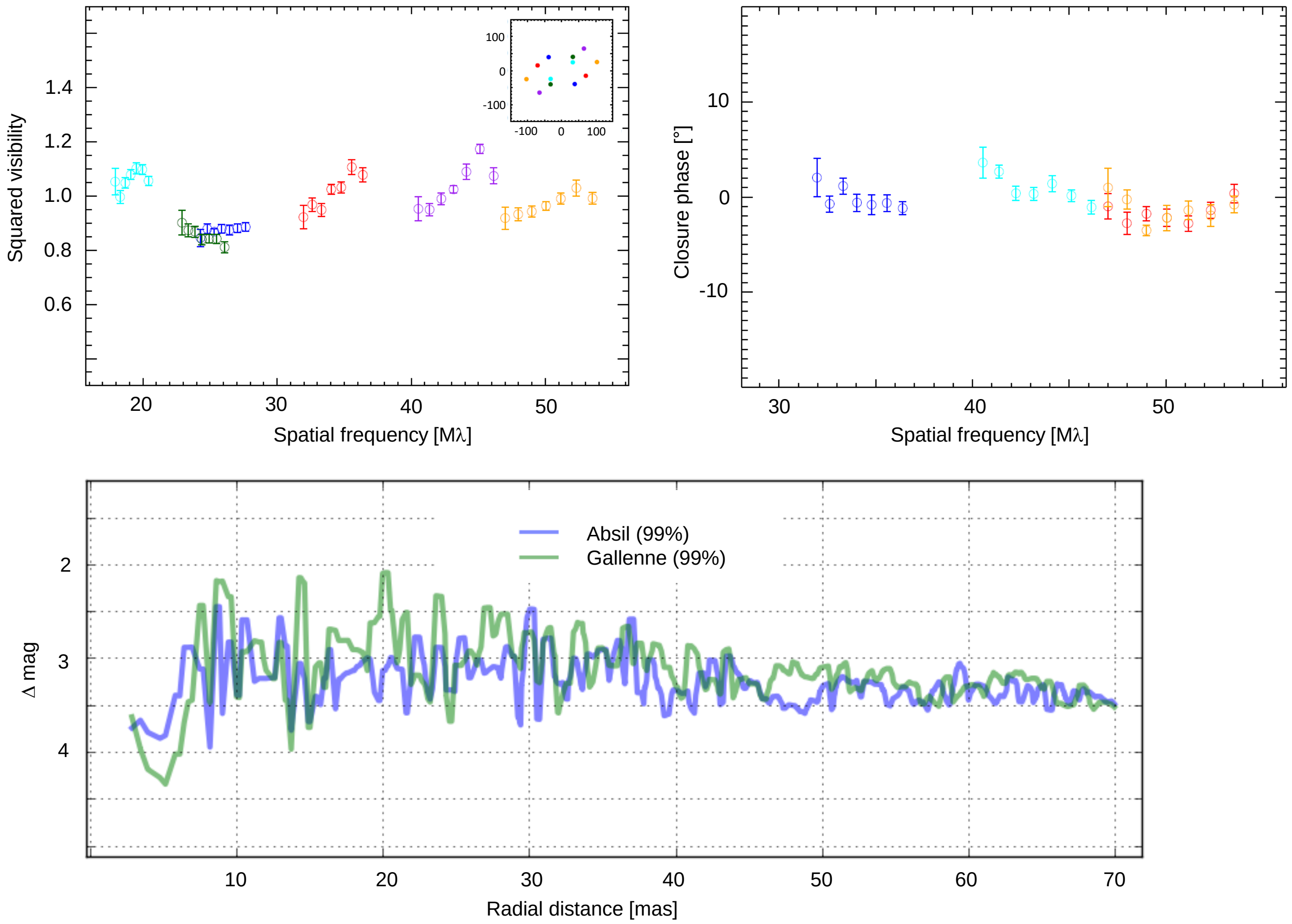

Fig. 21. Galactic center star S2: the *top panel* shows the observed squared visibilities and closure phases. The baseline coverage is shown in the small inset. The *bottom panel* displays the 3σ detection limit for companions of S2 as function of separation applying two different methods (Absil et al. 2011; Gallenne et al. 2015). Companions brighter than $\Delta m_K = 3$ mag, corresponding to a limiting magnitude of $m_K = 17.1$ mag, are ruled out.

for interferometry with all previous instruments. The observations of such faint objects are now possible with GRAVITY, because its fringe tracker can also work off-axis, and the stable performance allows us to increase the coherent integration time by orders of magnitude. We observed S2 with 10 s exposures at low spectral resolution ($R \approx 22$); the total integration time on source was 300 s. We debiased the data with a matching 300 s sky observation and calibrated the visibilities with GC IRS 16C observed with the same settings. The resulting visibilities and closure phases[6] of S2 are featureless (see Fig. 21). The closure phase scatters around zero with 1.7° rms. This is only marginally higher than the average closure phase error of 1° obtained from boot-strapping. This strongly indicates an unresolved source. The squared visibility shows more substructure than the closure phase. This is not surprising because the source is quite faint and therefore very sensitive to additive noise or imperfect bias subtraction, and the visibility is close to one and therefore very sensitive to the multiplicative noise from atmospheric piston residuals and coupling fluctuations. The mean squared visibility is 0.97 ± 0.09. There is no apparent drop at large spatial frequencies, which is again consistent with an unresolved source.

Because of the tidal field from Sgr A*, S2 cannot have physical companions that could be resolved with GRAVITY. The maximum separation for such companions is set by the tidal disruption radius, which for S2 is 0.24 mas, that is, smaller than the resolution of GRAVITY. The extremely dense stellar environment, however, can lead to chance associations with other stars in the field. We use two methods to determine the detection limits for such faint companions: the first method introduced by Absil et al. (2011) assumes that the data follows Gaussian statistics and compares the χ^2 of the null hypothesis with a companion model. The second method – CANDID (Gallenne et al. 2015) – injects fake companions into the data and tries to recover them. Figure 21 shows the resulting limits as a function of separation. We can rule out companions brighter than $\Delta m_K = 3$ mag, that is, $m_K < 17.1$ mag at a significance level of 3σ. The limiting magnitude of $m_K = 17.1$ mag corresponds to a B8V star at the Galactic center distance of 8.3 kpc (Gillessen et al. 2017) and K-band extinction of 2.7 mag (Fritz et al. 2011). Overall our observations already lead to a firm upper limit despite the short observing time and the consequently limited baseline coverage. Longer observations with a better baseline coverage will quickly lead to tighter constraints.

---

[6] Throughout the paper we use the longest baseline of the triangle to denote the spatial frequency of the closure phases.

3.5.3. First detection of Sgr A* in infrared interferometry

The compact radio source Sgr A* marks the position of the Galactic center black hole. The radio emission originates from the hot, ionized plasma of the inner accretion zone. On top of this quasi-steady component there is variable emission in the X-ray and infrared bands, which appears as flares, typically a few times per day and lasting for about 1−2 h (Baganoff et al. 2001; Genzel et al. 2003; Eckart et al. 2004; Eisenhauer et al. 2005). The flares originate from transiently heated electrons of the inner accretion and outflow region (Dodds-Eden et al. 2009), but the details are still under debate. Because any matter close to the black hole moves with a sizable fraction of the speed of light, GRAVITY will observe a motion of the flare if a single small region dominates its emission. If originating from close to the last stable orbit, the time variability and motion of the flares are directly tied to the mass and spin of the black hole. But it could also be that the flares come from a compact jet, thereby tracing the outflow dynamics of a supermassive black hole. If the flares reflect statistical fluctuations in the accretion flow, GRAVITY will observe no or random motion (Vincent et al. 2014). In any case the flares from the Galactic center are key to the understanding of the black hole's accretion physics, and thus are a prime target for GRAVITY.

Here we report on the first interferometric detection of an infrared flare from Sgr A* on 21 September 2016. We followed the flare for just over one hour until reaching the limit of the VLTI delay lines. The peak apparent brightness during our interferometric observations was $m_K \approx 15$ mag and the average brightness was about 0.5 mag fainter. The fringes from the flare are clearly detected in individual 10 s exposures. In total we could acquire 11 good data sets in low spectral resolution ($R \approx 22$), each containing 30 times 10 s exposures. We spent a total of 3300 s on source. The top panels of Fig. 22 show the visibilities and closure phases for one of the data sets. The prominent modulation of the visibility and closure phase with baseline length is the interferometric signature of the two brightest objects in the field, the flare from Sgr A* and the star S2. The black line shows the best fit model assuming two point sources. We repeat this "binary" fit for each of the 11 interferometric data sets to derive the K-band brightness ratio between Sgr A* and S2. This interferometric K-band lightcurve (Fig. 22 bottom) of Sgr A* follows closely the H-band lightcurve as measured from the acquisition and guiding camera images.

In order to uncover a potential substructure or additional point sources, we applied several image reconstruction algorithms to create maps of the surroundings of Sgr A*, including CLEAN (Högbom 1974), MiRA (Thiébaut 2008), and SQUEEZE (Baron et al. 2010). The various algorithms consistently recover Sgr A* and S2 in the images. Both objects are unresolved at the about 2 mas × 4 mas angular resolution of the VLTI. The middle left panel of Fig. 22 gives the example of the image reconstructed with MiRA for the combination of the three exposures of five minutes each around the peak of the flare. The spurious sources around Sgr A* and S2 are likely artifacts from the comparably sparse baseline coverage.

To quantify the detection limit for a third point source, we derive for each image point the necessary brightness for a 3σ detection of an artificial star when fitting a three object model to the full data set. The radial profile of the required contrast with Sgr A* is shown in the middle right panel of Fig. 22. Taking into account the mean flare brightness of $m_K \approx 15.5$ mag during our observations, we can exclude a third source brighter than $m_K \approx 17.1$ mag for 90% of the area within 50 mas radius around Sgr A* at the time of our observation. This limiting magnitude is quite comparable to the 3σ limit for the non-detection of chance companions of S2 in Sect. 3.5.2.

3.6. Dual-beam astrometry of the M-dwarf binary GJ 65

One of the key scientific applications of GRAVITY is narrow-angle astrometry. This technique is based on the simultaneous observation of two objects within the VLTI field-of-view (2″ and 4″ with UTs and ATs, respectively). The differential nature of the measurement removes most of the astrometric uncertainties. In principle this technique is only limited by the residual atmospheric disturbance between the two objects, which averages out with observing time. Among the first to recognize the potential of narrow-angle astrometry was Lindegren (1980). The application in interferometry was later proposed by Shao & Colavita (1992). They especially noted the possibility of micro-arcsecond astrometry using long baseline interferometry. In order to test and develop the GRAVITY dual-object astrometry, we observed a number of binaries with separations of a few arcseconds and magnitudes $m_K \approx 1$−7 mag.

The well studied M-dwarf binary GJ 65 AB (BL Cet+UV Cet, WDS J01388-1758AB) consists of two very low mass M5.5Ve and M6Ve main-sequence dwarfs with masses of $M(\mathrm{A}) = 0.123\,M_\odot$ and $M(\mathrm{B}) = 0.120\,M_\odot$ (Kervella et al. 2016). The two stars orbit each other with a period of $P = 26.28$ yr and a semi-major axis $a = 2.05''$. With a distance of only 2.68 pc, GJ 65 is one of the closest stars to the sun. The close proximity allowed Kervella et al. (2016) to measure the size with the VLTI. The best fit uniform disk diameter are $\theta(\mathrm{A}) = 0.56$ mas and $\theta(\mathrm{B}) = 0.54$ mas. Both components have almost equal brightness with $m_K(\mathrm{A}) = 6.02$ mag and $m_K(\mathrm{B}) = 6.17$ mag. They belong to the family of flare stars, which show violent outbursts of X-ray and UV radiation. Flares can significantly increase the UV brightness of M5V-stars, yet the K-band contribution is negligible at <1% (Davenport et al. 2012).

We observed GJ 65 AB repeatedly with the ATs in the A0-G1-J2-K0 configuration in August 2016, October 2016, and January 2017. Figure 23 shows the measured relative positions. We clearly detect an orbital motion, which we approximate with a quadratic fit to the positions. We derive the following motion: $\Delta\alpha(t) = 287.140 \pm 0.013\,\mathrm{mas} - (597.54 \pm 0.45\,\mu\mathrm{as/d}) \times (t - t_0) + (0.026 \pm 0.005\,\mu\mathrm{as/d}^2) \times (t - t_0)^2$ and $\Delta\delta(t) = 2258.142 \pm 0.028\,\mathrm{mas} + (35.92 \pm 0.97\,\mu\mathrm{as/d}) \times (t - t_0) - (0.132 \pm 0.006\,\mu\mathrm{as/d}^2) \times (t - t_0)^2$, with $t_0 = 57\,607.348$ (MJD). The individual fit errors are between 20−30 μas, about a factor two to three smaller than the actual scatter.

In principle, some of the scatter could be due to faint companions. However, the day-to-day scatter is about as large as the month-to-month scatter, therefore the residual scatter is more likely to originate from multiple systematic error sources. A detailed error analysis of the GRAVITY narrow-angle astrometry has been presented by Lacour et al. (2014). Some errors are related to the telescope array, for example, baseline instabilities from the AT relocations, flexure, pupil drifts, and pointing uncertainties. The active field guiding (Sect. 2.2.15) and pupil control (Sect. 2.2.16) already minimize several of these errors. However, we have not yet implemented a more advanced post processing of, for example, the acquisition camera data to correct for guiding residuals, and we have also not yet included the calibration of the narrow-angle astrometric baseline. Other error sources are related to the instrument, for example errors in the fiber positions, the dispersion of the single mode fibers and integrated optics, and the uncertainty in the wavelength calibration. We

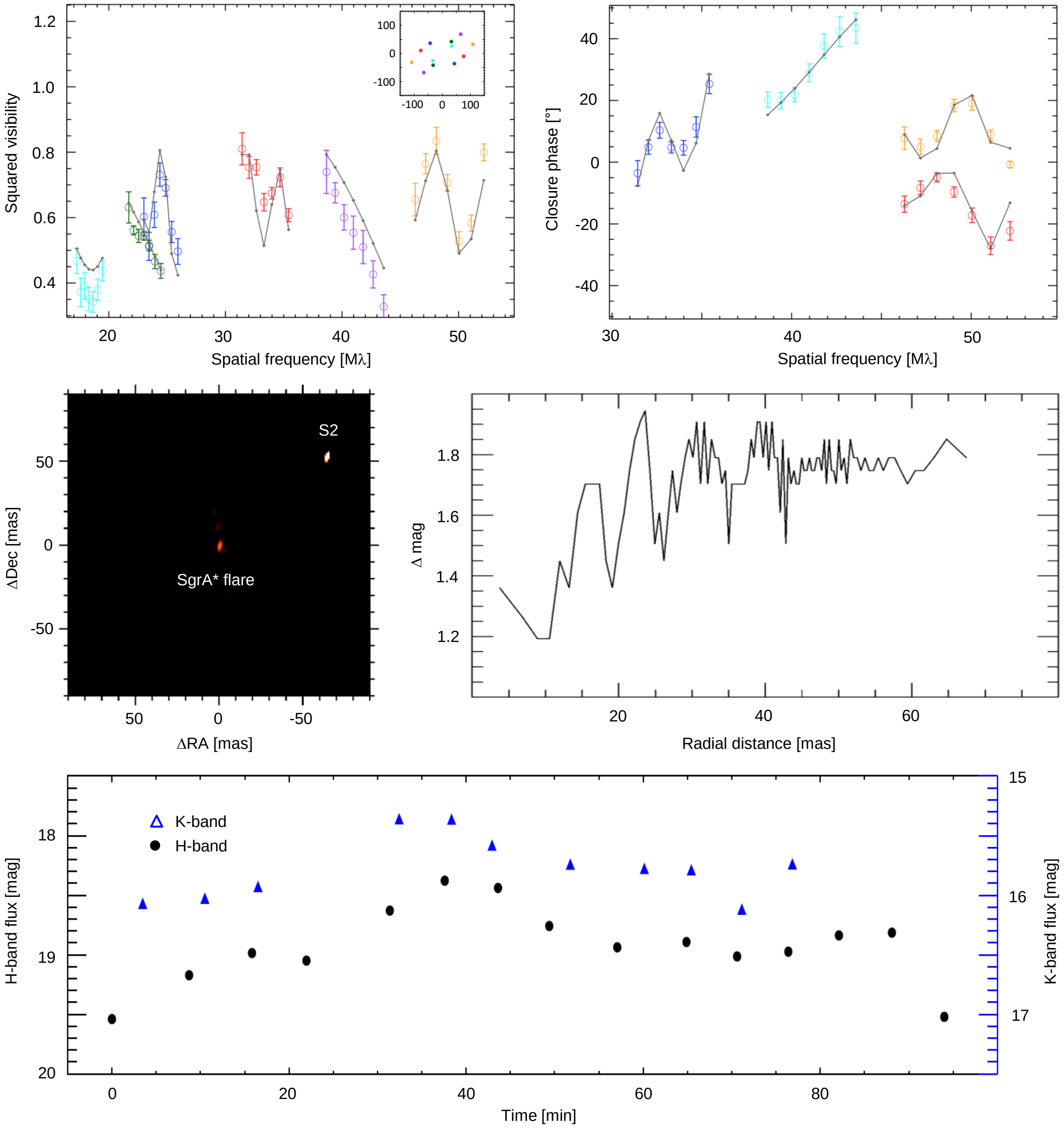

Fig. 22. First detection of Sgr A* in infrared interferometry: the *top panels* show the observed squared visibilities and closure phases for a five minute exposure centered on Sgr A* during a flare with a peak brightness of about $m_K \approx 15$ mag. The prominent modulation in the two quantities results from the two brightest objects in the field, the flaring Sgr A* and the star S2. The black line is the best fit "binary" model. The *middle left panel* displays the reconstructed image from the combination of three exposures around the peak of the flare. The *middle right panel* plots the 3σ detection limits for a third source in the full data set, for which the average flare brightness was $m_K \approx 15.5$ mag. We can exclude a third source brighter than $m_K = 17.1$ mag for 90% of the area. The *lower panel* shows the *H*-band (black circles) and *K*-band (blue triangles) lightcurve of Sgr A* during the flare, as measured from the acquisition camera images and derived from the best fit to the interferometric visibilities and closure phases, respectively.

already include the dispersion in our analysis. We have made significant progress in the wavelength calibration and we are currently exploring possibilities to improve the fiber positioning and object acquisition. The last family of errors to be mentioned here are related to the laser metrology and the effects of non-common path aberrations and polarization on the path-length measurement. Also here we are still in the process of transferring the theoretical concepts into the actual data analysis and calibration. The upcoming commissioning runs will concentrate on these aspects to further improve GRAVITY's narrow-angle astrometry towards the goal of 10 μas accuracy.

4. Summary

GRAVITY and the VLTI set new standards in optical/infrared interferometry. Our first observations demonstrate fringe-tracking

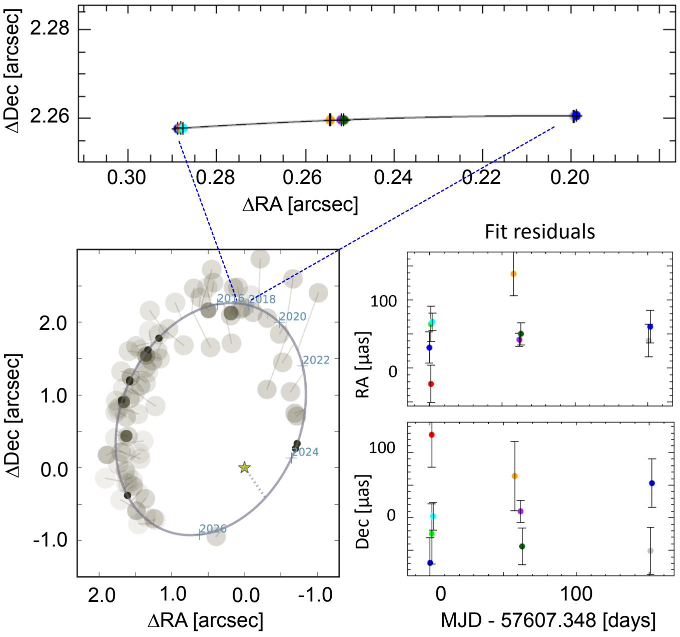

Fig. 23. Dual-beam astrometry of the M-dwarf binary GJ 65: the *top panel* shows the astrometry from three observing epochs in 2016 and the best quadratic fit (black) to the GRAVITY data. The *lower left panel* displays the orbit of GJ 65 from Kervella et al. (2016) based on seeing limited and adaptive optics observations. On the *lower right* we plot the residuals for the best quadratic fit to the GRAVITY astrometry. The mean rms scatter is 42 μas and 64 μas in right ascension and declination, respectively.

on unresolved stars as faint as $m_K \approx 10$ mag, coherent exposures on objects fainter than $m_K \approx 15$ mag, limiting magnitudes of $m_K \approx 17$ mag, visibility accuracies better than 0.25% and closure phase accuracy better than 0.5°, multi-wavelength interferometric imaging with a spectral resolution of $R \approx 4500$, spectro-differential astrometry with a few μas precision, and dual-field astrometry with 50 μas residuals.

The breakthrough with GRAVITY – especially with respect to the observations of faint objects – is best illustrated with the comparison to previous limits: before GRAVITY, the so-far faintest object observed with near-infrared interferometry – as part of the technical dual-field phase-referencing instrument demonstration with the Keck telescopes – was $m_K = 12.5$ mag (Woillez et al. 2014), a factor of ten brighter than the flare from the Galactic center black hole discussed in the previous chapter. The difference is even a factor of 100 when compared with previously published science observations, for which the faintest objects had an apparent brightness around $m_K \approx 10.1$ mag (Weigelt et al. 2012) and $m_K \approx 10.2$ mag (Kishimoto et al. 2011) with the VLTI and Keck Interferometer, respectively. For fringe-tracking – a prerequisite for long-exposures and high spectral resolution interferometry – GRAVITY is increasing the sensitivity of the VLTI by a factor of ten compared to what is possible with FINITO, for which the *H*-band limiting magnitude for phase-tracking is $m_H \approx 7.5$ mag. The limiting magnitude records of GRAVITY make a whole new range of objects accessible to optical/infrared interferometry.

At the same time, GRAVITY can be used without specific interferometry expertise, comes with a science grade data reduction software, and is offered to the world-wide community through the European Southern Observatory. Although the Galactic center is the key science target for GRAVITY, the instrument enables the study of many other objects, both with the ATs and UTs.

This paper demonstrates the unique capabilities and performance of GRAVITY with a number of notable firsts, including the first observation of the Galactic center supermassive black hole and its fast orbiting star S2 with infrared interferometry, the first interferometric observations of a T Tauri star and a HMXB at high spectral resolution, the first 10 μas spectro-differential interferometry of a quasar broad line region, and the first dual-field interferometric astrometry with residuals as low as 50 μas.

Acknowledgements. Based on observations made with ESO Telescopes at the La Silla Paranal Observatory under programme IDs 60.A-9102 and 099.B-0162. We thank the technical, administrative, and scientific staff of the participating institutes and the observatory for their extraordinary support during the development, installation, and commissioning of GRAVITY. The instrument relies strongly on the VLTI infrastructure, and we want to especially express thanks for its timely upgrade to prepare for GRAVITY. Since July 2008, the work on the spectrometers of GRAVITY has been supported in part by the German Federal Ministry for Education and Research (BMBF) under the grants Verbundforschung #05A08PK1 #05A11PK2 & #05A14PKA. G. Perrin and K. Perraut acknowledge the support of Agence Nationale de la Recherche contract #ANR-06-BLAN-0421, LabEx OSUG@2020 (Investissements d'avenir – ANR10LABX56), Action Spécifique ASHRA of CNRS/INSU and CNES, Action Spécifique GRAM of CNRS/INSU-INP and CNES. S. Gillessen and C. Deen acknowledge the support from ERC starting grant No. 306311. O. Pfuhl acknowledges the support from ERC synergy grant No. 610058 "BlackHoleCam: Imaging the Event Horizon of Black Holes". S. Lacour acknowledges support from ERC starting grant No. 639248. J. Sanchez-Bermudez acknowledges the support from the Alexander von Humboldt Foundation Fellowship programme (Grant number ESP 1188300 HFST-P). The Portuguese participation in GRAVITY was partially funded by Fundação para a Ciência e Tecnologia with grants PTDC/CTE-AST/116561/2010, COMPETE FCOMP-01-0124-FEDER-019965, UID/FIS/00099/2013 and SFRH/BD/52066/2012. This research was partially funded by the European Community's Seventh Framework Programme, under Grant Agreements 226604 and 312430 (OPTICON Fizeau Programme), and has made use of the Jean-Marie Mariotti Center `Aspro`, `OIFits Explorer` and `SearchCal` services and of CDS Astronomical Databases SIMBAD and VIZIER.

References

Absil, O., Le Bouquin, J.-B., Berger, J.-P., et al. 2011, A&A, 535, A68
Abuter, R., Dembet, R., Lacour, S., et al. 2016, in Optical and Infrared Interferometry and Imaging V, Proc. SPIE, 9907, 990721
Alef, W. 1989, in NATO Advanced Science Institutes (ASI) Series C, 283, eds. M. Felli, & R. E. Spencer, 261
Amorim, A., Lima, J., Anugu, N., et al. 2012, in Optical and Infrared Interferometry III, Proc. SPIE, 8445, 844534
Anthonioz, F., Ménard, F., Pinte, C., et al. 2015, A&A, 574, A41
Anugu, N., Garcia, P. J. V., Wieprecht, E., et al. 2014, in Optical and Infrared Interferometry IV, Proc. SPIE, 9146, 91462C
Arsenault, R., Alonso, J., Bonnet, H., et al. 2003, in Adaptive Optical System Technologies II, eds. P. L. Wizinowich, & D. Bonaccini, Proc. SPIE, 4839, 174
Baade, D., Balestra, A., Cumani, C., et al. 2009, The Messenger, 136, 20
Baganoff, F. K., Bautz, M. W., Brandt, W. N., et al. 2001, Nature, 413, 45
Ballester, P., Bramich, D., Forchi, V., et al. 2014, in Astronomical Data Analysis Software and Systems XXIII, eds. N. Manset, & P. Forshay, ASP Conf. Ser., 485, 11
Baron, F., Monnier, J. D., & Kloppenborg, B. 2010, in Optical and Infrared Interferometry II, Proc. SPIE, 7734, 77342I
Bauvir, B., Wallander, A., Duhoux, P., Huxley, A., & Karban, R. 2004, in Advanced Software, Control, and Communication Systems for Astronomy, eds. H. Lewis, & G. Raffi, Proc. SPIE, 5496, 155
Blind, N., Eisenhauer, F., Haug, M., et al. 2014, in Optical and Infrared Interferometry IV, Proc. SPIE, 9146, 91461U
Blondin, J. M. 1994, ApJ, 435, 756
Bonaccini, D., Gallieni, D., Biasi, R., et al. 1997, in Adaptive Optics and Applications, eds. R. K. Tyson, & R. Q. Fugate, Proc. SPIE, 3126, 580
Burtscher, L., Wieprecht, E., Ott, T., et al. 2014, in Optical and Infrared Interferometry IV, Proc. SPIE, 9146, 91462B
Čechura, J., & Hadrava, P. 2015, A&A, 575, A5
Choquet, É., Menu, J., Perrin, G., et al. 2014, A&A, 569, A2

Colavita, M. M., & Wizinowich, P. L. 2003, in Interferometry for Optical Astronomy II, ed. W. A. Traub, Proc. SPIE, 4838, 79

Colavita, M. M., Wallace, J. K., Hines, B. E., et al. 1999, ApJ, 510, 505

Coudé du Foresto, V., Perrin, G., Ruilier, C., et al. 1998, in Astronomical Interferometry, ed. R. D. Reasenberg, Proc. SPIE, 3350, 856

Cumani, C., Balestra, A., & Stegmeier, J. 2006, in Astrophys. Space Sci. Lib., 336, eds. J. E. Beletic, J. W. Beletic, & P. Amico, 589

Dai, X., Hippler, S., & Gendron, E. 2017, J. Mod. Opt., 64, 127

Davenport, J. R. A., Becker, A. C., Kowalski, A. F., et al. 2012, ApJ, 748, 58

Deen, C., Kolb, J., Oberti, S., et al. 2016, in Adaptive Optics Systems V, Proc. SPIE, 9909, 99092M

Delplancke, F. 2008, New Astron. Rev., 52, 199

Delplancke, F., Nijenhuis, J., de Man, H., et al. 2004, in New Frontiers in Stellar Interferometry, ed. W. A. Traub, Proc. SPIE, 5491, 1528

Derie, F. 2000, in Interferometry in Optical Astronomy, eds. P. Léna, & A. Quirrenbach, Proc. SPIE, 4006, 25

Dodds-Eden, K., Porquet, D., Trap, G., et al. 2009, ApJ, 698, 676

Duvert, G., Young, J. S., & Hummel, C. 2016, in Optical and Infrared Interferometry and Imaging V, Proc. SPIE, 9907, 990710

Eckart, A., Baganoff, F. K., Morris, M., et al. 2004, A&A, 427, 1

Eisenhauer, F., Genzel, R., Alexander, T., et al. 2005, ApJ, 628, 246

Eisenhauer, F., Perrin, G., Rabien, S., et al. 2008, in The Power of Optical/IR Interferometry: Recent Scientific Results and 2nd Generation, eds. A. Richichi, F. Delplancke, F. Paresce, & A. Chelli, 431

Eisenhauer, F., Perrin, G., Brandner, W., et al. 2011, The Messenger, 143, 16

ESO 2012, GASGANO: Data File Organizer, Astrophysics Source Code Library

Fedrigo, E., Donaldson, R., Soenke, C., et al. 2006, in SPIE Conf. Ser., Proc. SPIE, 6272, 627210

Finger, G., Dorn, R. J., Eschbaumer, S., et al. 2008, in High Energy, Optical, and Infrared Detectors for Astronomy III, Proc. SPIE, 7021, 70210P

Finger, G., Baker, I., Alvarez, D., et al. 2014, in Adaptive Optics Systems IV, Proc. SPIE, 9148, 914817

Finger, G., Baker, I., Alvarez, D., et al. 2016, in Adaptive Optics Systems V, Proc. SPIE, 9909, 990912

Fizeau, H. 1868, C. R. Acad. Sci., 66, 932

Fritz, T. K., Gillessen, S., Dodds-Eden, K., et al. 2011, ApJ, 737, 73

Gai, M., Corcione, L., Lattanzi, M. G., et al. 2003, Mem. Soc. Astron. It., 74, 472

Gallenne, A., Mérand, A., Kervella, P., et al. 2015, A&A, 579, A68

Genzel, R., Schödel, R., Ott, T., et al. 2003, Nature, 425, 934

Genzel, R., Eisenhauer, F., & Gillessen, S. 2010, Rev. Mod. Phys., 82, 3121

Ghez, A. M., Salim, S., Weinberg, N. N., et al. 2008, ApJ, 689, 1044

Gillessen, S., Plewa, P. M., Eisenhauer, F., et al. 2017, ApJ, 837, 30

Gitton, P. B., Leveque, S. A., Avila, G., & Phan Duc, T. 2004, in New Frontiers in Stellar Interferometry, ed. W. A. Traub, Proc. SPIE, 5491, 944

Gonté, F., Woillez, J., Schuhler, N., et al. 2016a, in Optical and Infrared Interferometry and Imaging V, Proc. SPIE, 9907, 99071Z

Gonté, F. Y. J., Alonso, J., Aller-Carpentier, E., et al. 2016b, in Optical and Infrared Interferometry and Imaging V, Proc. SPIE, 9907, 990720

GRAVITY Collaboration, Petrucci, P.-O., Waisberg, I., et al. 2017a, A&A, in press, DOI: 10.1051/0004-6361/201731038

GRAVITY Collaboration, Waisberg, I., Dexter, J., et al. 2017b, ApJ, submitted [`arXiv:1705.02351`]

Gull, T. R., Madura, T. I., Groh, J. H., & Corcoran, M. F. 2011, ApJ, 743, L3

Gull, T. R., Madura, T. I., Teodoro, M., et al. 2016, MNRAS, 462, 3196

Haberl, F. 1991, ApJ, 376, 245

Haguenauer, P., Abuter, R., Andolfato, L., et al. 2012, in Optical and Infrared Interferometry III, Proc. SPIE, 8445, 84450D

Hale, D. D. S., Bester, M., Danchi, W. C., et al. 2000, ApJ, 537, 998

Hargrave, P. J., & Ryle, M. 1974, MNRAS, 166, 305

Haubois, X., Perrin, G., Lacour, S., et al. 2009, A&A, 508, 923

Haug, M., Haussmann, F., Kellner, S., et al. 2012, in Optical and Infrared Interferometry III, Proc. SPIE, 8445, 84452V

Hestroffer, D. 1997, A&A, 327, 199

Högbom, J. A. 1974, A&AS, 15, 417

Jocou, L., Perraut, K., Nolot, A., et al. 2012, in Optical and Infrared Interferometry III, Proc. SPIE, 8445, 84452X

Jocou, L., Perraut, K., Moulin, T., et al. 2014, in Optical and Infrared Interferometry IV, Proc. SPIE, 9146, 91461J

Johnson, M. A., Betz, A. L., & Townes, C. H. 1974, Phys. Rev. Lett., 33, 1617

Kaper, L., van der Meer, A., & Najarro, F. 2006, A&A, 457, 595

Kervella, P., Mérand, A., Ledoux, C., Demory, B.-O., & Le Bouquin, J.-B. 2016, A&A, 593, A127

Kiekebusch, M. J., Lucuix, C., Erm, T. M., et al. 2014, in Software and Cyberinfrastructure for Astronomy III, Proc. SPIE, 9152, 915207

Kishimoto, M., Hönig, S. F., Antonucci, R., et al. 2011, A&A, 527, A121

Kraus, S., Kluska, J., Kreplin, A., et al. 2017, ApJ, 835, L5

Labeyrie, A. 1975, ApJ, 196, L71

Lachaume, R. 2003, A&A, 400, 795

Lacour, S., Meimon, S., Thiébaut, E., et al. 2008, A&A, 485, 561

Lacour, S., Eisenhauer, F., Gillessen, S., et al. 2014, A&A, 567, A75

Lane, B. F., & Muterspaugh, M. W. 2004, ApJ, 601, 1129

Lapeyrere, V., Kervella, P., Lacour, S., et al. 2014, in Optical and Infrared Interferometry IV, Proc. SPIE, 9146, 91462D

Lazareff, B., Berger, J.-P., Kluska, J., et al. 2017, A&A, 599, A85

Le Bouquin, J.-B., Berger, J.-P., Lazareff, B., et al. 2011, A&A, 535, A67

Le Bouquin, J.-B., Sana, H., Gosset, E., et al. 2017, A&A, 601, A34

Leahy, D. A., & Kostka, M. 2008, MNRAS, 384, 747

Leveque, S. A., Wilhelm, R., Salvade, Y., Scherler, O., & Daendliker, R. 2003, in Interferometry for Optical Astronomy II, ed. W. A. Traub, Proc. SPIE, 4838, 983

Lindegren, L. 1980, A&A, 89, 41

Lippa, M., Gillessen, S., Blind, N., et al. 2016, in Optical and Infrared Interferometry and Imaging V, Proc. SPIE, 9907, 990722

Lopez, B., Lagarde, S., Jaffe, W., et al. 2014, The Messenger, 157, 5

Madura, T. I., Gull, T. R., Okazaki, A. T., et al. 2013, MNRAS, 436, 3820

McKay, D. J., Ballester, P., Banse, K., et al. 2004, in Optimizing Scientific Return for Astronomy through Information Technologies, eds. P. J. Quinn, & A. Bridger, Proc. SPIE, 5493, 444

Menu, J., Perrin, G., Choquet, E., & Lacour, S. 2012, A&A, 541, A81

Mérand, A., Bordé, P., & Coudé du Foresto, V. 2005, A&A, 433, 1155

Michelson, A. A., & Pease, F. G. 1921, ApJ, 53

Monnier, J. D., Berger, J.-P., Le Bouquin, J.-B., et al. 2014, in Optical and Infrared Interferometry IV, Proc. SPIE, 9146, 91461Q

Netzer, H. 2015, ARA&A, 53, 365

Ott, T., Wieprecht, E., Burtscher, L., et al. 2014, in Optical and Infrared Interferometry IV, Proc. SPIE, 9146, 91462A

Paumard, T., Genzel, R., Martins, F., et al. 2006, ApJ, 643, 1011

Paumard, T., Perrin, G., Eckart, A., et al. 2008, in The Power of Optical/IR Interferometry: Recent Scientific Results and 2nd Generation, eds. A. Richichi, F. Delplancke, F. Paresce, & A. Chelli, 313

Pearson, T. J., Unwin, S. C., Cohen, M. H., et al. 1981, Nature, 290, 365

Perrin, G., Coudé du Foresto, V., Ridgway, S. T., et al. 1998, A&A, 331, 619

Perrin, G., Ridgway, S. T., Mennesson, B., et al. 2004, A&A, 426, 279

Petrov, R. G., Malbet, F., Weigelt, G., et al. 2007, A&A, 464, 1

Pfuhl, O., Haug, M., Eisenhauer, F., et al. 2014, in Optical and Infrared Interferometry IV, Proc. SPIE, 9146, 914623

Pozna, E., Zins, G., Santin, P., & Beard, S. 2008, in Advanced Software and Control for Astronomy II, Proc. SPIE, 7019, 70190Q

Prato, L., Greene, T. P., & Simon, M. 2003, ApJ, 584, 853

Press, W. H., Teukolsky, S. A., Vetterling, W. T., & Flannery, B. P. 2002, Numerical recipes in C++: the art of scientific computing (Cambridge University Press)

Quirrenbach, A., Mozurkewich, D., Buscher, D. F., Hummel, C. A., & Armstrong, J. T. 1994, A&A, 286, 1019

Rakshit, S., Petrov, R. G., Meilland, A., & Hönig, S. F. 2015, MNRAS, 447, 2420

Reeves, J. N., O'Brien, P. T., Vaughan, S., et al. 2000, MNRAS, 312, L17

Scheithauer, S., Brandner, W., Deen, C., et al. 2016, in Adaptive Optics Systems V, Proc. SPIE, 9909, 99092L

Schödel, R., Ott, T., Genzel, R., et al. 2002, Nature, 419, 694

Shao, M., & Colavita, M. M. 1992, A&A, 262, 353

Shao, M., & Staelin, D. H. 1980, Appl. Opt., 19, 1519

Shao, M., Colavita, M. M., Hines, B. E., et al. 1988, A&A, 193, 357

Stephan, E. C. R. 1874, Compt. Rend. Acad. Sci. (Paris), 78, 1008

Straubmeier, C., Yazici, S., Wiest, M., et al. 2014, in Optical and Infrared Interferometry IV, Proc. SPIE, 9146, 914629

Tatulli, E., Millour, F., Chelli, A., et al. 2007, A&A, 464, 29

Thiébaut, E. 2008, in Optical and Infrared Interferometry, Proc. SPIE, 7013, 70131I

Thiébaut, É. 2013, in EAS Pub. Ser., 59, eds. D. Mary, C. Theys, & C. Aime, 157

Thompson, A. R., Moran, J. M., & Swenson, Jr., G. W. 2017, Interferometry and Synthesis in Radio Astronomy, 3rd edn. (John Wiley & Sons)

van Boekel, R., Kervella, P., Schöller, M., et al. 2003, A&A, 410, L37

Vincent, F. H., Paumard, T., Perrin, G., et al. 2014, MNRAS, 441, 3477

Vural, J., Kreplin, A., Kraus, S., et al. 2012, A&A, 543, A162

Weigelt, G., Petrov, R. G., Chesneau, O., et al. 2006, in Society of Photo-Optical Instrumentation Engineers (SPIE) Conference Series, Proc. SPIE, 6268, 62682S

Weigelt, G., Hofmann, K.-H., Kishimoto, M., et al. 2012, A&A, 541, L9

Weigelt, G., Hofmann, K.-H., Schertl, D., et al. 2016, A&A, 594, A106

Woillez, J., & Lacour, S. 2013, ApJ, 764, 109

Woillez, J., Wizinowich, P., Akeson, R., et al. 2014, ApJ, 783, 104

Yang, P., Hippler, S., Deen, C. P., et al. 2013, Optics Express, 21, 9069

---

[1] Max Planck Institute for extraterrestrial Physics, Giessenbachstr., 85748 Garching, Germany
[2] LESIA, Observatoire de Paris, PSL Research University, CNRS, Sorbonne Universités, UPMC Univ. Paris 06, Univ. Paris Diderot, Sorbonne Paris Cité, 92195 Meudon Cedex, France
[3] Max-Planck-Institut für Astronomie, Königstuhl 17, 69117 Heidelberg, Germany
[4] 1. Physikalisches Institut, Universität zu Köln, Zülpicher Str. 77, 50937 Köln, Germany
[5] Univ. Grenoble Alpes, CNRS, IPAG, 38000 Grenoble, France
[6] CENTRA and Universidade de Lisboa – Faculdade de Ciências, Campo Grande, 1749-016 Lisboa, Portugal
[7] CENTRA and Universidade do Porto – Faculdade de Engenharia, 4200-465 Porto, Portugal
[8] European Southern Observatory, Karl-Schwarzschild-Str. 2, 85748 Garching, Germany
[9] European Southern Observatory, Casilla 19001, Santiago 19, Chile
[10] Observatoire de Genève, Université de Genève, 51 Ch. des Maillettes, 1290 Versoix, Switzerland
[11] Onera – The French Aerospace Lab, BP 72, 92 322 Châtillon, France
[12] European Space Agency, Space Telescope Science Institute, 3700 San Martin Drive, Baltimore, MD 21218, USA
[13] Unidad Mixta Internacional Franco-Chilena de Astronomía (CNRS UMI 3386), Departamento de Astronomía, Universidad de Chile, Camino El Observatorio 1515, Las Condes, Santiago, Chile
[14] Max-Planck-Institute for Radio Astronomy, Auf dem Hügel 69, 53121 Bonn, Germany
[15] Sterrewacht Leiden, Leiden University, Postbus 9513, 2300 RA Leiden, The Netherlands
[16] Department of Physics, Le Conte Hall, University of California, Berkeley, CA 94720, USA